Influence of soil microstructure on air permeability in compacted clay

V. Nguyen[1], J.A. Pineda[1*], E. Romero[2] & D. Sheng[3]

[1] Priority Research Centre for Geotechnical Science and Engineering, School of Civil and Environmental Engineering, the University of Newcastle Australia, Callaghan Campus, EA Building, 2308, Newcastle NSW, Australia

[2] Department of Geotechnical Engineering and Geosciences, Technical University of Catalonia, UPC, Campus Nord, Building D2, 08034, Barcelona, Spain

[3] School of Civil and Environmental Engineering, University of Technology Sydney, City Campus, Sydney, Australia (formerly at the University of Newcastle Australia)

[*] Corresponding author: jubert.pineda@newcastle.edu.au , Ph: +61 2 49217034

Abstract

This paper describes an experimental study aimed at evaluating the influence of soil microstructure on air permeability in compacted clay. Air permeability measurements, estimated using the gas pressure decay method, were carried out for a wide range of compaction states. The evolution of the air permeability during wetting and drying paths was also evaluated. The experimental results show that, for an increase in the as-compacted degree of saturation, air permeability may either increase or decrease depending on the as-compacted dry density. Air permeability increases with increasing the degree of saturation in loose specimens whereas the opposite trend is observed for dense specimens. Microstructural analysis, carried out using Mercury Intrusion Porosimetry (MIP) tests, shows a strong dependency of the air permeability on the as-compacted soil microstructure, even for specimens that experienced large variation in degree of saturation. The variation of the air permeability in wetted and dried specimens shows an opposite trend compared to as-compacted samples, for similar dry density and degree of saturation. Microstructural data indicate that air permeability is mainly controlled by large pores that display high connectivity. The degree of saturation plays a dual role on soil microstructure which, in turn, affects the air permeability. Denser specimens (dry density ≥ 1.5 Mg/m^3) show a reduction in k_{eff} due to the expansion of the clay aggregates with increasing the as-compacted degree of saturation. The increase in the as-compacted degree of saturation in loose samples (dry density ≤ 1.3 Mg/m^3) produces an enhancement in the proportion of macro pores, thus increasing k_{eff}, as a consequence of modifications in the PSD. There is a threshold value above which further increase in the degree of saturation causes a reduction in the proportion of macro pores, therefore in k_{eff}. A new proposal for estimating the air permeability is proposed in this paper based on the determination of a pore size parameter (PSP) obtained from MIP data. The proposed approach seems capable of describing the evolution of air permeability for the whole spectrum of compaction states, including specimens subjected to wetting and drying paths.

1. Introduction

The influence of soil microstructure (fabric) in engineering practice was early recognized by Terzaghi (1925) and Casagrande (1932). However, it was only about three decades later when its dependency on the mechanical behaviour of compacted clays was (indirectly) confirmed using laboratory test results (Lambe, 1953; Leonards, 1955; Lambe, 1958a,b; Seed & Chan, 1959; Mitchell, 1965; among others). Since then, further developments in microstructural testing techniques have allowed the multi-scale characterization of compacted soils including the detailed evaluation of the arrangement and distribution of particles and/or aggregates as well as their assembly and connectivity (e.g., Barden & Sides, 1970; Sridharan et al., 1971; Barden et al., 1973; McGown & Collins, 1975; Osipov & Sokolov, 1978; García-Bengoechea et al., 1979; Delage et al., 1996; Tarantino & De Col, 2008; Monroy et al., 2010; Romero, 2013; among others).

Various attempts have been made over the last decades to link soil microstructure with pore fluid permeability (water and gas) in compacted soils using the pore size distribution (PSD) estimated from mercury intrusion porosimetry (MIP) data (e.g., García-Bengoechea et al., 1979; Juang & Holtz, 1986; Romero, 2013; Zhan et al., 2014). Although relative success has been demonstrated in soils with dominant mono-modal pore size distribution, issues have been recognized when these approaches are applied to clayey materials with dominant multi-modal PSD which evolves depending on mechanical as well as environmental actions. The relationship between the clay microstructure and the unsaturated hydraulic properties is complex and may not be properly captured by existing models, in particular when important variations in void ratio (dry density) and water content are considered (Liu et al. 2014; Chen et al. 2017). The lack of proper methodologies for estimating unsaturated permeability increases the uncertainty related to the design and performance of engineering barriers systems (EBS) such as municipal solids waste landfills and radioactive waste repositories (e.g., Vanpaisal and Bouazza, 2004; Juca and Maciel, 2006; Olivella & Alonso, 2008; Zhan et al., 2014; Rouf et al. 2016; He et al., 2017). Within this context, important efforts have been made over the last two decades to improve our understanding of the role of soil microstructure on gas flow through unsaturated clayey geomaterials (e.g., Villar et al., 2005; Romero et al., 2005; Olivella & Alonso, 2008; Romero, 2013).

In line with that approach, this paper presents the results of an experimental investigation aimed at evaluating the influence of the as-compacted microstructure on air permeability. Air permeability is evaluated for a wide spectrum of dry densities and water contents (degrees of saturation). Air permeability tests are complemented with mercury intrusion porosimetry (MIP)

tests, carried out on as-compacted specimens and samples exposed to wetting and drying paths, in order to link microstructural features to air permeability. An attempt is made here to propose a unified approach, based on pore size distribution data obtained from MIP tests, capable to represent the evolution of air permeability with soil microstructure even for specimens exposed to wetting and drying paths.

2. Experimental techniques

2.1. Air permeability tests

Air permeability was evaluated in a stress-path triaxial apparatus adapted to allow air injection tests according to the procedure described in Pineda et al. (2014). The experimental layout is shown in Figure 1. In this set-up, a pressurized tank of known volume V and at an initial absolute pressure p_0 (upstream vessel) is connected to the bottom cap, whereas the top cap is maintained under atmospheric conditions (downstream absolute pressure at p_{atm}). The time evolution of the absolute air pressure decay p_t inside the tank is recorded, which can be used to estimate the mass of air flowing through the sample assuming perfect gas law. The expression derived by Yoshimi & Osterberg (1963), based on the generalized Darcy's law for compressible fluid and the perfect gas law, was adopted in this study to estimate the (effective) air permeability of compacted specimens:

$$k_{eff}[m^2] = \left[\frac{2.30 V h \mu_a}{A\left(p_{atm}+\frac{p_0}{4}\right)}\right]\left[\frac{-\log_{10}\left(\frac{p_t}{p_0}\right)}{t}\right] \quad (1)$$

where V is volume of the air tank, h and A are the height and cross-section area of soil specimen, respectively, μ_a is the air dynamic viscosity and p_{atm} is the atmospheric pressure. p_t and p_0 refer to the gauge pressure in the tank at time t and t = 0, respectively.

Although several approaches have been used in the past, the concept of effective air permeability, k_{eff}, is adopted in following sections to consider the contribution of partial saturation (S_r) effects, porosity (density) effects as well as changes in the PSD due to microstructural effects. In the following sections, it will be noted that the role of the degree of saturation on soil microstructure, and therefore on gas flow, is twofold. An increase in S_r may cause a reduction in gas flow (and k_{eff}) due to the occlusion of soil pores by either the expansion of clay aggregates and/or the filling of soil pores with liquid water. On the other hand, an increase in S_r may also change the soil microstructure (i.e. the structural arrangement of the

clay aggregates), therefore the PSD, leading to either increase or decrease the gas flow through the specimen. Examples of this behaviour are given below.

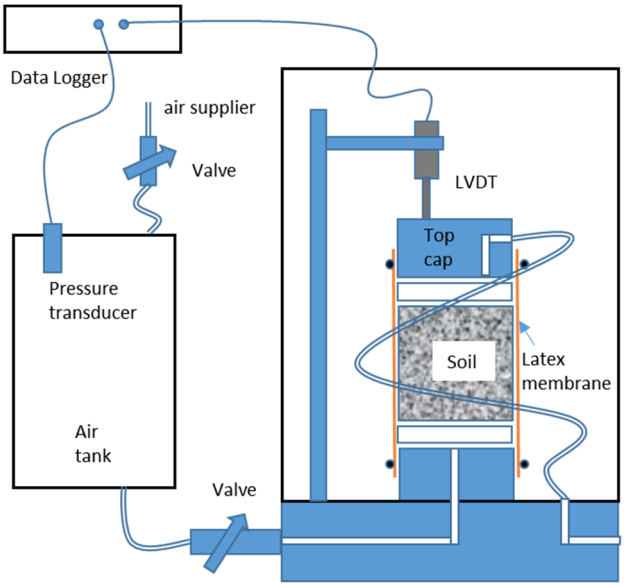

Figure 1. Experimental set-up for air permeability tests

2.2. Mercury intrusion porosimetry (MIP)

Mercury Intrusion Porosimetry (MIP) tests were used to evaluate the pore size distribution (PSD) of specimens used in the air permeability tests. The principle of MIP is based on the Washburn equation (Washburn, 1921), which relates the applied mercury injection pressure *p* to an equivalent entrance pore size *d*, as described by Eq. 2:

$$p = -\frac{4\sigma_{mercury}\cos\theta_{nw}}{d} \quad (2)$$

where $\sigma_{mercury}$ is the surface tension of mercury (0.484 N/m at 25 °C, as adopted by Diamond, 1970; Delage & Lefebvre, 1984) and θ_{nw} is the mercury-soil contact angle (assumed equal to 140° as adopted by Romero & Simms (2008)). Values of the void ratio associated with intruded mercury are computed from the test results obtained during the intrusion stage as $e_{MIP} = V_{mercury}/V_{solids}$, where V_{solids} is the volume of the dry solids used for the MIP test and $V_{mercury}$ is the cumulative volume of intruded mercury at the current pressure. The pore size density (PSD) function is estimated from the derivative of the cumulative intrusion curve according to:

$$f(\log x_m) = -\frac{\delta(e_{MIP})}{\delta(\log d)} \quad (3)$$

where $\log(x_m)$ is the midpoint of the pore diameter class.

MIP tests were carried out using an AutoPore IV 9500 porosimeter (Micromeritics®). The mercury intrusion pressure incrementally increased to the maximum value of 228 MPa (minimum entrance pore diameter of approximately 6.5 nm) using an intrusion rate of 0.001 mL/g.s. MIP tests were performed on small cubical sub-samples (≈ 5 mm side) trimmed from specimens previously subjected to air permeability tests. Freeze drying was first applied to the MIP samples as recommended by Delage & Pellerin (1984), among others. After treatment, the specimens were sealed in airtight plastic bottles and stored in a desiccator prior to microstructural analysis.

3. Material and specimen preparation

Commercial kaolin Q38 (Sibelco®, Australia), composed by 95% kaolinite and 5% quartz, is the soil used in this study. It has a liquid limit of 51 %, a plastic limit of 29 % and an average density of solid particles of 2.63 Mg/m^3. Specimens were compacted by mixing dry powder kaolinite with distilled water. The mixture was sieved to produce a maximum aggregate size of 2.36 mm. An equalization time of 48 h was allowed to the mixture prior compaction. Cylindrical specimens, 50 mm in diameter and 50 mm in height, were statically compacted under a displacement rate of 1.5 mm/min. Specimens were compacted in five layers to minimize density variations. The evolution of total vertical stress and void ratio during compaction were estimated using a load cell and one LVDT, respectively. Tests reported in this paper were performed at room temperature (20 ± 0.5 ^{o}C).

4. Experimental program

A total of 65 air permeability tests were carried out in this study on specimens compacted to dry densities, ρ_d, of 1.1, 1.3, 1.5, 1.6 and 1.7 Mg/m^3 and water contents, w, ranging from 2.5 % to 33 % (i.e., 10 < S_r < 89 %). A summary of the compaction states is given in Table 1, including specimens exposed to wetting and drying paths. Two specimens per compaction state were typically subjected to air permeability testing. Figure 2 shows the compaction plane (ρ_d vs *w*) in which solid circles indicate the compaction conditions of tested specimens. Dashed lines represent constant values of net vertical stress (total vertical stress over air pressure: σ_v-u_a) required to achieve the target compaction states. Net vertical stresses between 0.07 MPa and 21.1 MPa were measured during compaction. It can be noted that, for specimens compacted to similar dry density (void ratio), the net vertical stress reduces with increasing the water content (i.e., with S_r).

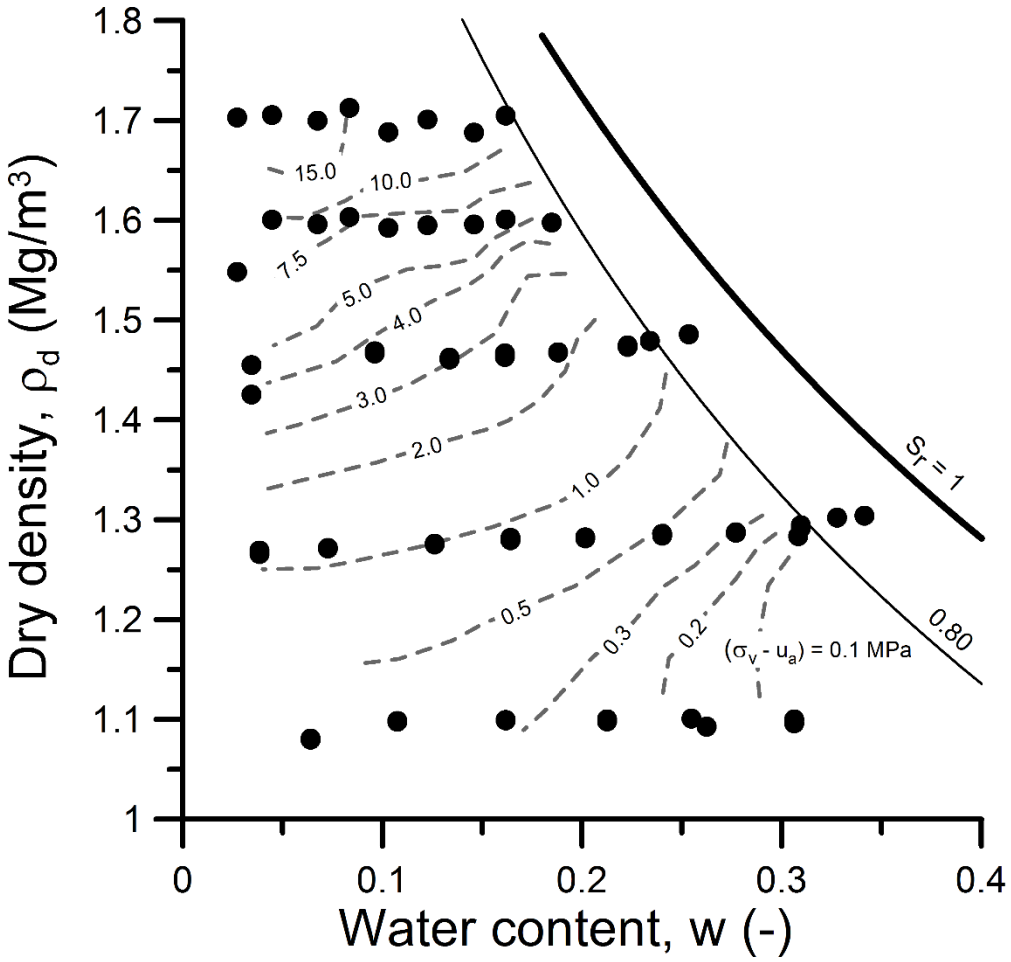

Figure 2. Compaction states

Each air permeability test included four stages: (i) isotropic loading, (ii) equalization, (iii) air injection phase, and (iv) isotropic unloading. Specimens were isotropically loaded to a mean net stress p-u_a = 50 kPa (u_a = p_{atm}) under a stress rate of 1 kPa/min. The target mean net stress was selected to be lower than the compaction net vertical stress in order to minimize variations in soil microstructure caused by plastic deformation. Axial deformation was monitored during the tests using a submergible mini LVDT (see Figure 1). Specimens were then equilibrated during 10-15 min prior the air injection phase. Afterwards, a gas pulse with an initial air pressure of p_0 = 40 kPa was applied through the bottom cap and the variation of the air pressure inside the tank was recorded. Specimens were then unloaded isotropically and final measures of total mass and volume were taken to assess variations in volumetric variables.

Figure 3 shows the air pressure decay curves $\log_{10}(p_t/p_0)$ vs time for specimens compacted to dry densities of 1.1 Mg/m^3 and 1.7 Mg/m^3. A clear influence of the compacted density and the degree of saturation is observed on the air pressure decay curves. Almost full dissipation of the air pressure was recorded after 500 s in loosest specimens whereas only 50% reduction was registered in denser specimens after 4.5 h. Although it may be less clear for denser

specimens, the testing time reduced with increasing the as-compacted S_r (water content). When clay powder has access to water clay aggregates may be formed. Previous evidence has indicated that soil microstructure will saturate first due to the high water absorption capacity of the clay platelets (e.g., Romero & Simms, 2008; Alonso et al., 2013). Therefore, increasing the water content (and S_r) will tend to form clay aggregates with larger sizes as their water adsorption capacity have been fulfilled. Figure 2 shows that less net vertical stress is required to compact specimens to the same dry density (e=cte) when increasing Sr. This behaviour would suggests the creation of an open microstructure (large pore voids). A discussion of this phenomenon within the context of the gas flow phenomenon is given in following sections.

Figure 4 shows the variation of the axial strain during air permeability tests for specimens reported in Figure 3. The isotropic loading caused axial compression with values ranging from 0.27 % to 0.35 % (loose specimens: $S_r \leq 1.3$ Mg/m^3) and between 0.125 % and 0.175 % (dense specimens: $S_r > 1.3$ Mg/m^3). Axial compression increased with increasing S_r. The largest compression strain (0.68 %) was recorded in a loose specimen compacted to $S_r = 60$ %, which was expected to have high compressibility due to its low compaction stress (0.07 MPa). Upward air flow was adopted during the air injection stage. It caused an initial axial swelling which vanished with decreasing air pressure inside the tank. With the exception of the loose specimen mentioned above, the remaining axial strain at the end of the air permeability test was less than 0.10 % (see Figure 4). Measures of initial volume (as-compacted) and final volume (after air permeability tests) were used to evaluate the volumetric strain ε_{vol} as shown in Figure 5 (note that most tests have been duplicated for consistency). Volumetric strain increases with increasing S_r although this response is clearer in specimens compacted to 1.1 Mg/m^3 and 1.3 Mg/m^3. The mean value for all tested specimens is 0.15 %, with lower values measured in denser specimens ($\rho_d \geq 1.5$ Mg/m^3).

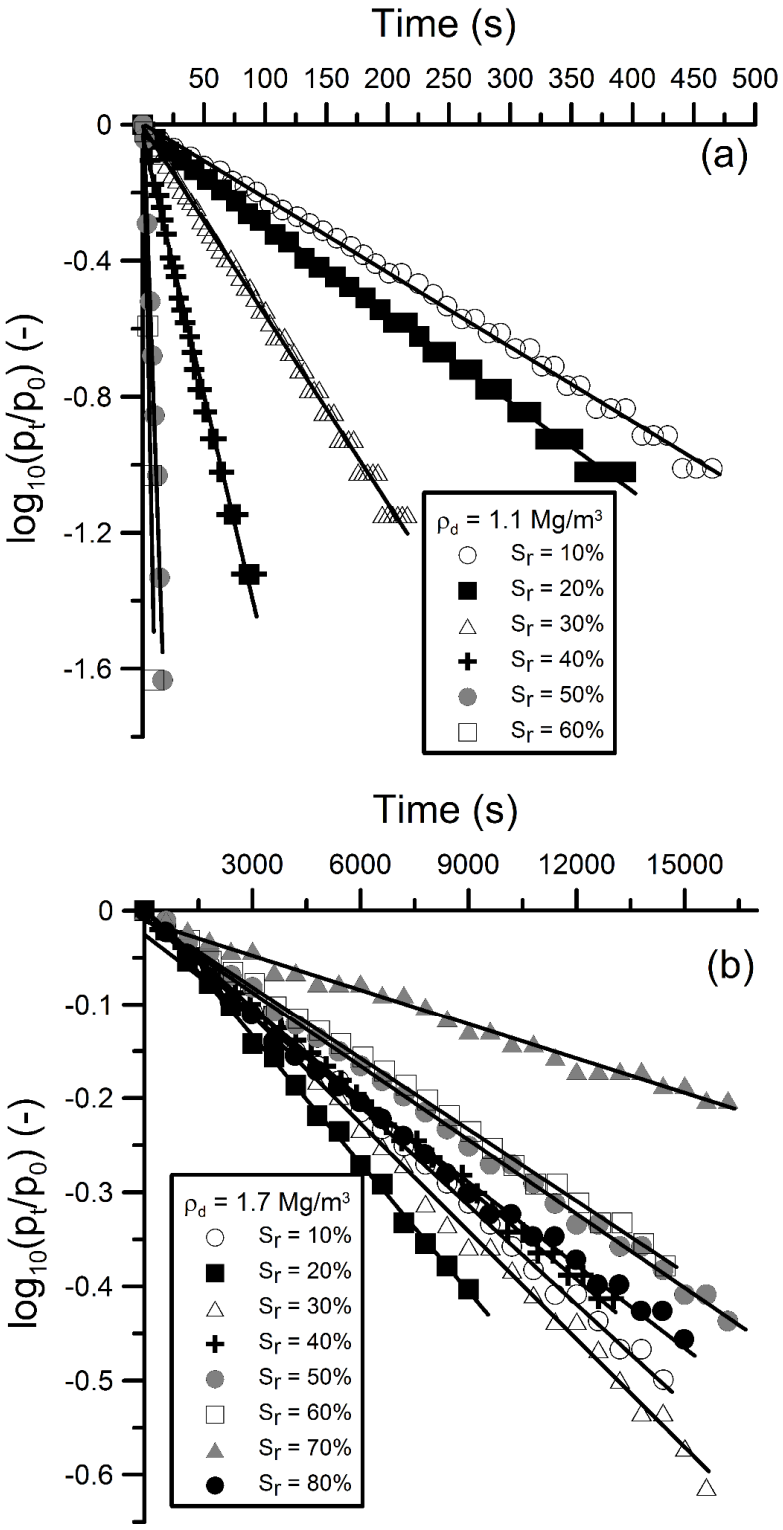

Figure 3. Pressure decay curves for specimens compacted to 1.1 Mg/m^3 (a) and 1.7 Mg/m^3 (b).

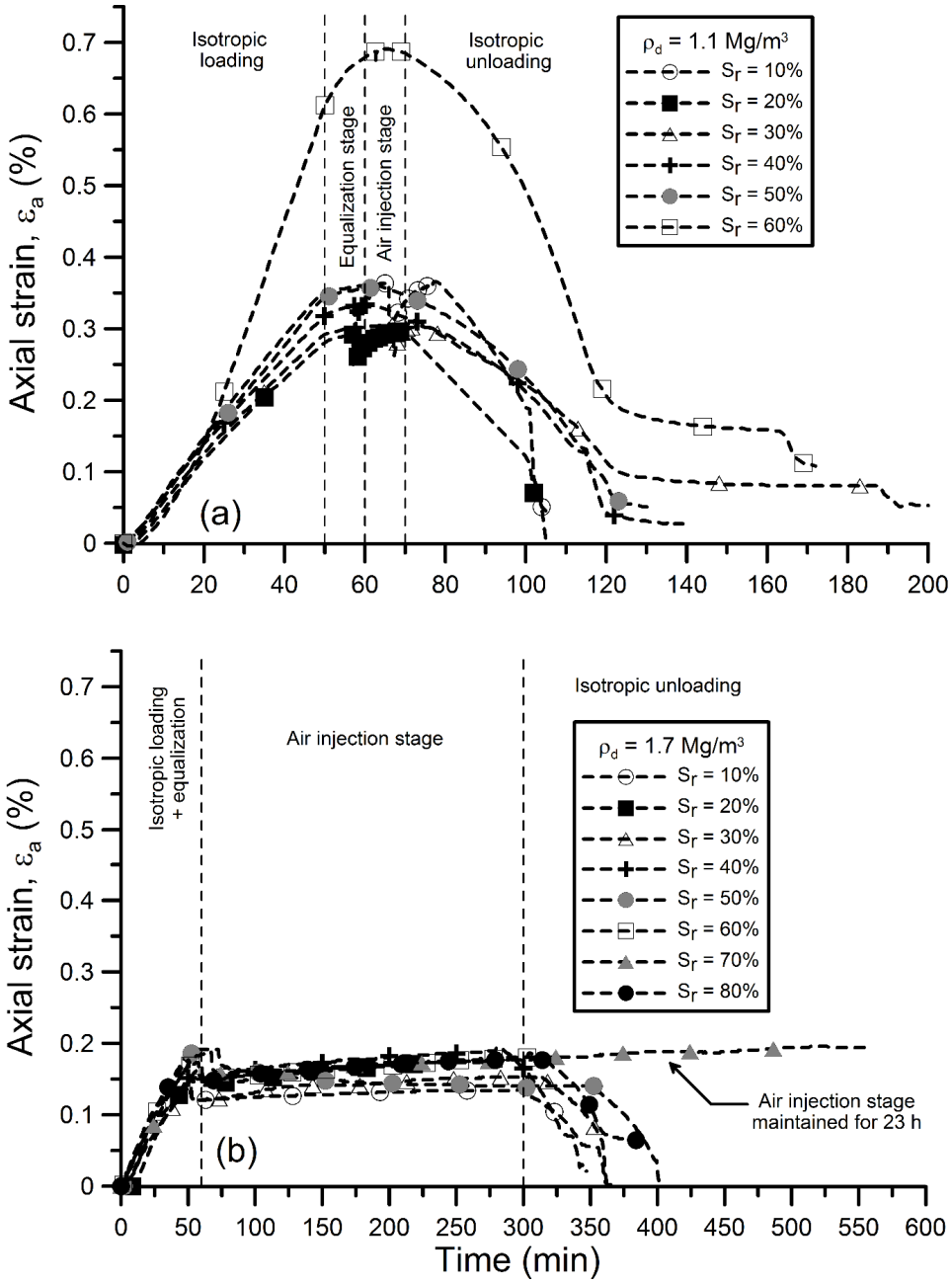

Figure 4. Variation of axial strain with time during air permeability tests for specimens compacted to 1.1 Mg/m^3 (a) and 1.7 Mg/m^3 (b).

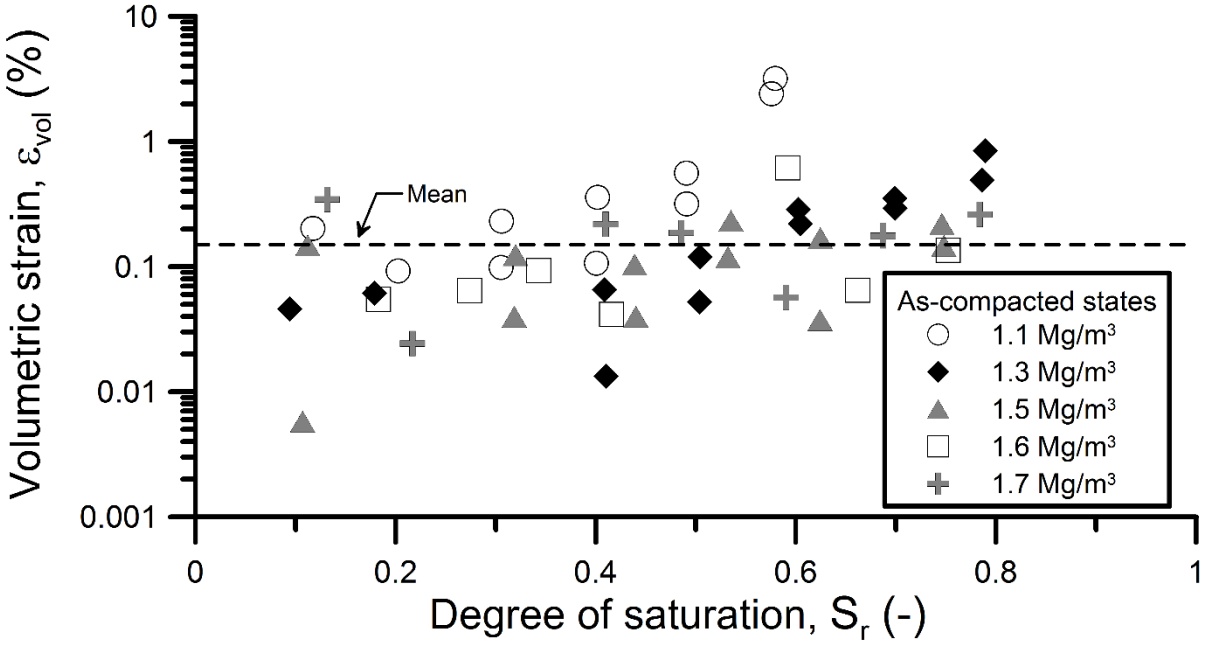

Figure 5. Volumetric deformation caused by isotropic loading during air permeability tests as a function of the as-compacted degree of saturation

5. Results

Figure 6 shows the variation of the effective air permeability, k_{eff}, with the as-compacted degree of saturation, S_r. Opposite trends are observed depending on the compaction density. Specimens compacted to dry densities lower or equal to 1.3 Mg/m^3 show a non-linear increase in k_{eff} with S_r, from 10^{-15} m^2 to 10^{-12} m^2. For the lowest compaction density, the maximum S_r achieved (without inducing collapse) is 60%. On the other hand, effective air permeability reduces with increasing S_r, from 10^{-15} m^2 to 10^{-17} m^2 in specimens compacted to dry densities higher than 1.3 Mg/m^3. It can be noted that the reduction in k_{eff} is clearer for S_r > 60% irrespective of the compaction density. As discussed in following sections, this threshold value is associated with modifications in the pore size density (PSD) of the compacted specimens.

The variation of k_{eff} with air void ratio, $e_a = e(1-S_r)$, is shown in Figure 7. According to its definition, e_a reduces with increasing S_r for specimens compacted to a given density. It implies less accessible air voids for gas flow as a consequence of increasing the amount of water in the soil microstructure (at constant void ratio). Under this scenario, it would be plausible to expect a reduction in k_{eff} with decreasing e_a (i.e., increasing S_r). The fact that such a response is only observed in dense specimens ($\rho_d \geq 1.5$ Mg/m^3) indicates that a macroscopic variable like e_a is not sufficient to describe the variation of k_{eff} with density and S_r. Hence, microstructural information like the PSD should be considered as it seems strongly influenced by variations in S_r. The weakness of macroscopic approaches for describing the evolution of k_{eff} is illustrated

in Figure 7. There, a power law model is used to fit the experimental results. Macroscopic power law models have been proposed to describe the variation of air permeability with air void ratio as: $k_{eff}=A.e_a^B$, where A and B are fitting parameters which seem to vary with ρ_d and global S_r (e.g., Yoshimi & Osterberg, 1963; Moldrup et al., 2003; Chamindu et al., 2011; Zhan et al., 2014; among others). In Figure 7, solid and dashed lines represent two ways of fitting the experimental results, depending on how the experimental data are grouped. The solid line represents the variation of k_{eff} with e_a for samples compacted to the same water content (w=25%) whereas the dashed line refers to specimens with the same dry density (void ratio). Although better fitting is obtained in the latter case, there is clear that such a model does not provide additional insights on the physical phenomenon controlling air permeability.

Experimental results presented above describe the variation of the effective air permeability for a wide range of as-compacted states. In practice, as-compacted conditions are also affected by moisture variations due to environmental actions. Hence, it is important to evaluate how does the effective air permeability change during wetting and drying paths but also if its variation is in agreement with the evolution of effective air permeability observed for as-compacted states.

To answer these questions, additional samples were compacted and subjected to controlled wetting or drying paths prior air permeability testing. Wetting and drying paths were controlled by pure diffusion using the vapour transfer technique (Blatz et al., 2008; Delage et al., 2008) under unstressed conditions. Periodic volume and weight measurements were used to determine the volumetric path followed by each specimen. Figures 8-12 show the evolution of k_{eff} with S_r and e_a for those specimens. Solid lines represent the variation of k_{eff} for the as-compacted specimens described above. Empty and grey circles refer here to effective air permeability measured during wetting and drying paths, respectively. Black circles represent the as-compacted states for the dry density under study. Numbers in brackets indicate the evolution of dry density during the hydraulic path. Figure 8 shows the evolution of k_{eff} with S_r for five additional samples (1.1 Mg/m^3), four wetted and one dried. Wetting cause a progressive reduction in k_{eff} irrespective of the initial S_r. The decrease in k_{eff} is attributed in this case to the expansion of clayey aggregates in addition to the accumulated volumetric compression caused during each isotropic loading stage prior air injection. This led to an increase in dry density from 1.1 up to 1.22 Mg/m^3. Interestingly, k_{eff} for wetted specimens is lower than values measured in samples compacted to 1.3 Mg/m^3. On the contrary, drying increases k_{eff} around two orders of magnitude with respect to the as-compacted states (1.3 Mg/m^3), for the same S_r. Figure 9 shows the variation of k_{eff} for two specimens compacted to the same dry density (1.3 Mg/m^3) at different initial degrees of saturation. The driest specimen (S_{r0} = 8%) was then wetted

until reach $S_r \approx 86\%$ whereas a reduction in S_r to 5% was applied to the specimen compacted at $S_{r0}=80\%$. Effective air permeability decreases around two orders of magnitude during wetting. However, almost negligible variation in k_{eff} is observed for $S_r < 60\%$ which is inconsistent with the trend defined by as-compacted samples. The value of k_{eff} at the end of the wetting path (10^{-17} m^2) is even lower than the measured in specimens compacted to dry densities of 1.7 Mg/m^3. Slight increase in k_{eff} is observed in the specimen exposed to drying, which is three orders of magnitude larger than the k_{eff} measured in samples compacted to 1.5 Mg/m^3 at similar S_r. These results show an opposite trend in Figures 8 and 9 between as-compacted states and values estimated for wetted and dried specimens (at similar S_r or e_a).

Figures 10-12 show that k_{eff} reduces during wetting in denser specimens (> 1.5 Mg/m^3), particularly when $S_r > 60\%$. This behaviour is in agreement with the results shown in Figures 6 and 7 for as-compacted specimens. Despite this similitude, the decrease in k_{eff} is, in this case, accompanied by a reduction in dry density due to swelling. Drying increases k_{eff} irrespective of the reduction in dry density. This behaviour is in agreement with the results presented previously in Figures 8 and 9. The variation of k_{eff} is, however, much larger in denser specimens (around two orders of magnitude).

In summary, effective air permeability reduces during wetting and increases with drying, irrespective of the compaction density. This behaviour is inconsistent with the as-compacted data, particularly for specimens compacted to dry densities lower than 1.3 Mg/m^3. The reduction of k_{eff} with decreasing dry density upon wetting observed in denser specimens is also inconsistent with the response of as-compacted specimens. These results suggest strong influence of S_r on the as-compacted microstructure and its subsequent evolution during wetting and drying (i.e., the modification of the PSD).

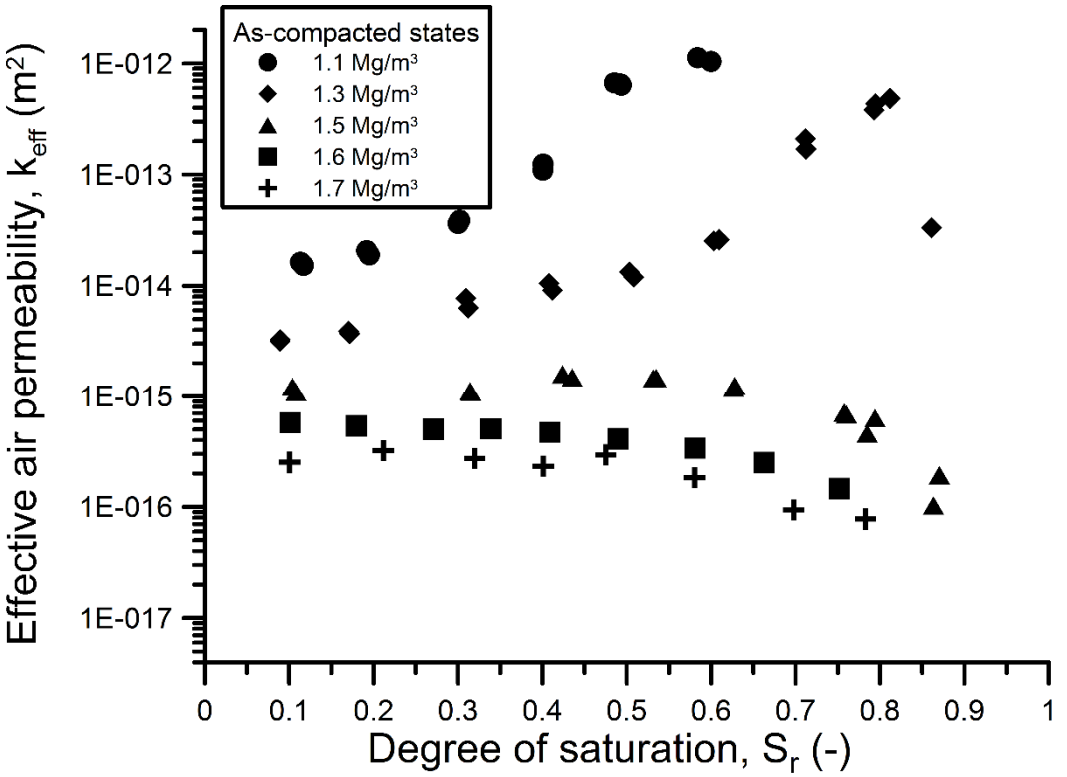

Figure 6. Variation of the effective air permeability with the degree of saturation for as-compacted specimens

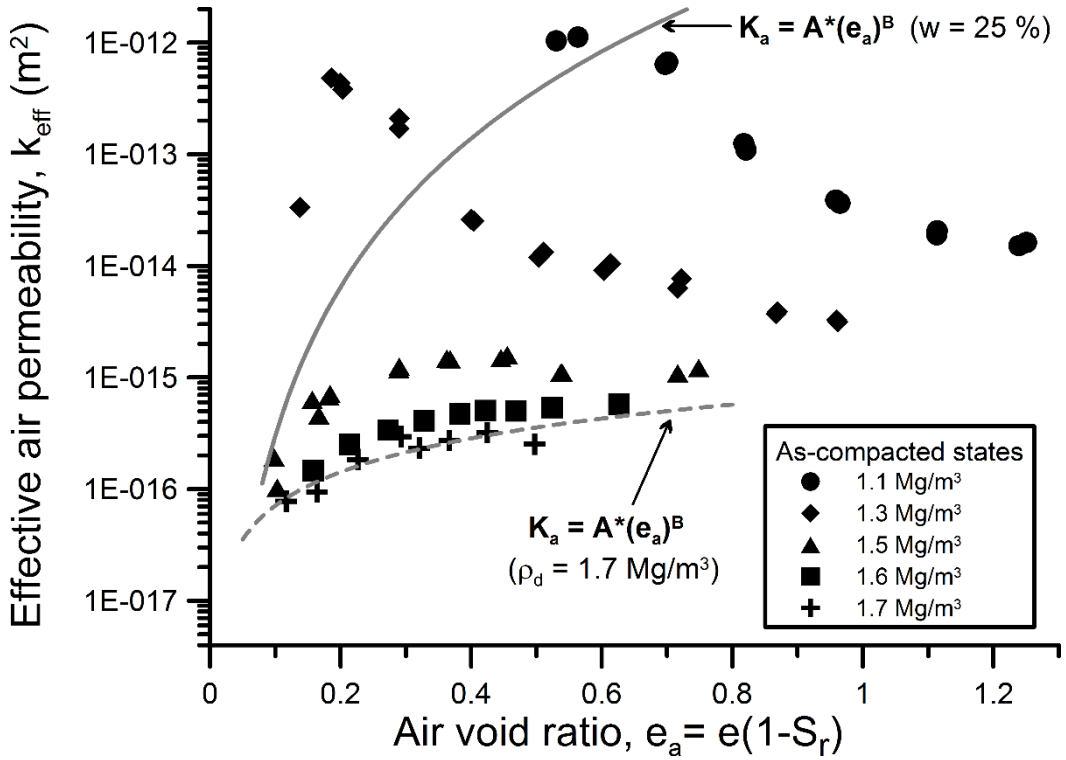

Figure 7.Variation of the effective air permeability with air void ratio for as-compacted specimens

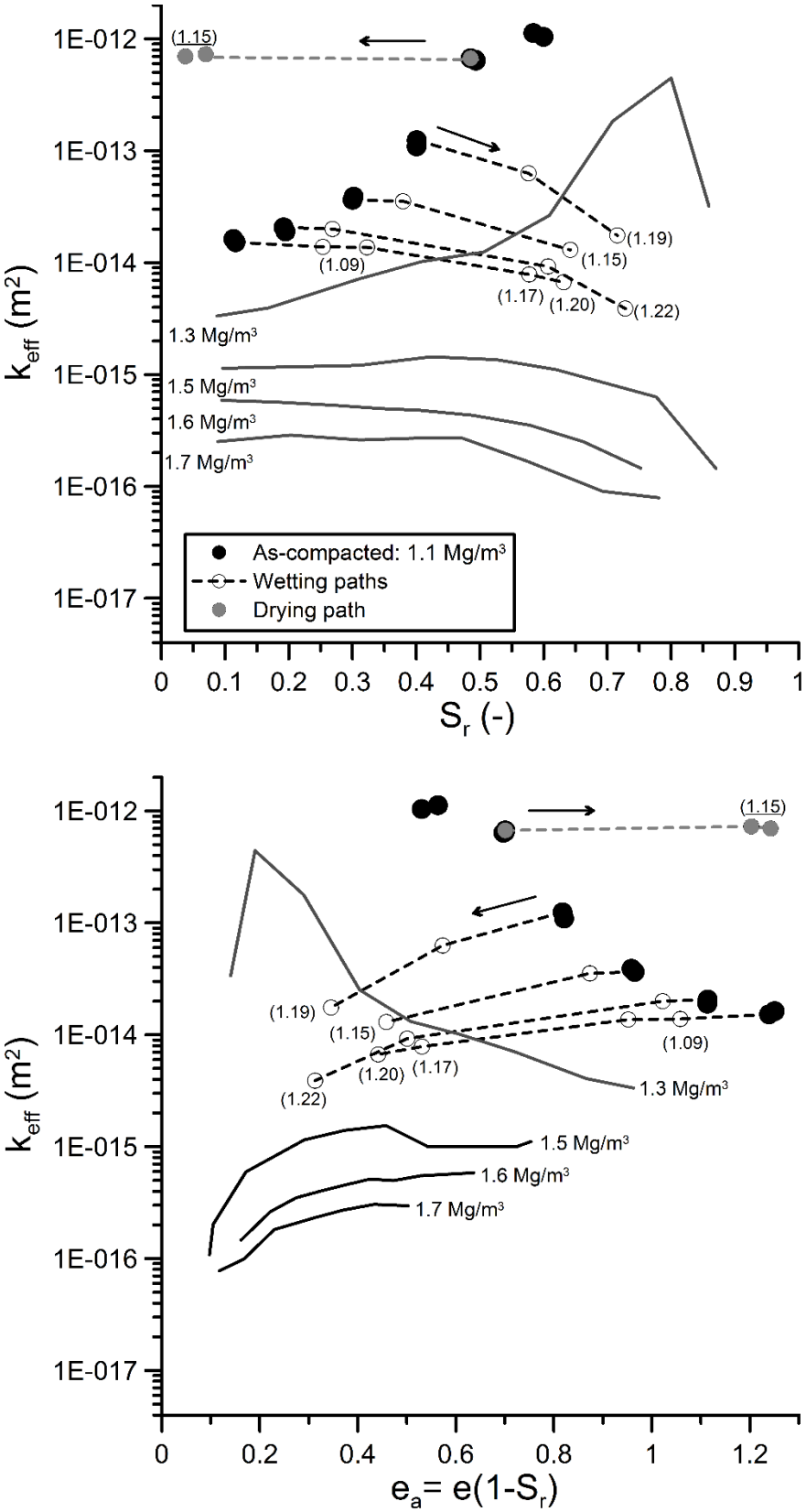

Figure 8.Evolution of k_{eff} with S_r and e_a during wetting and drying for specimens compacted to 1.1 Mg/m3

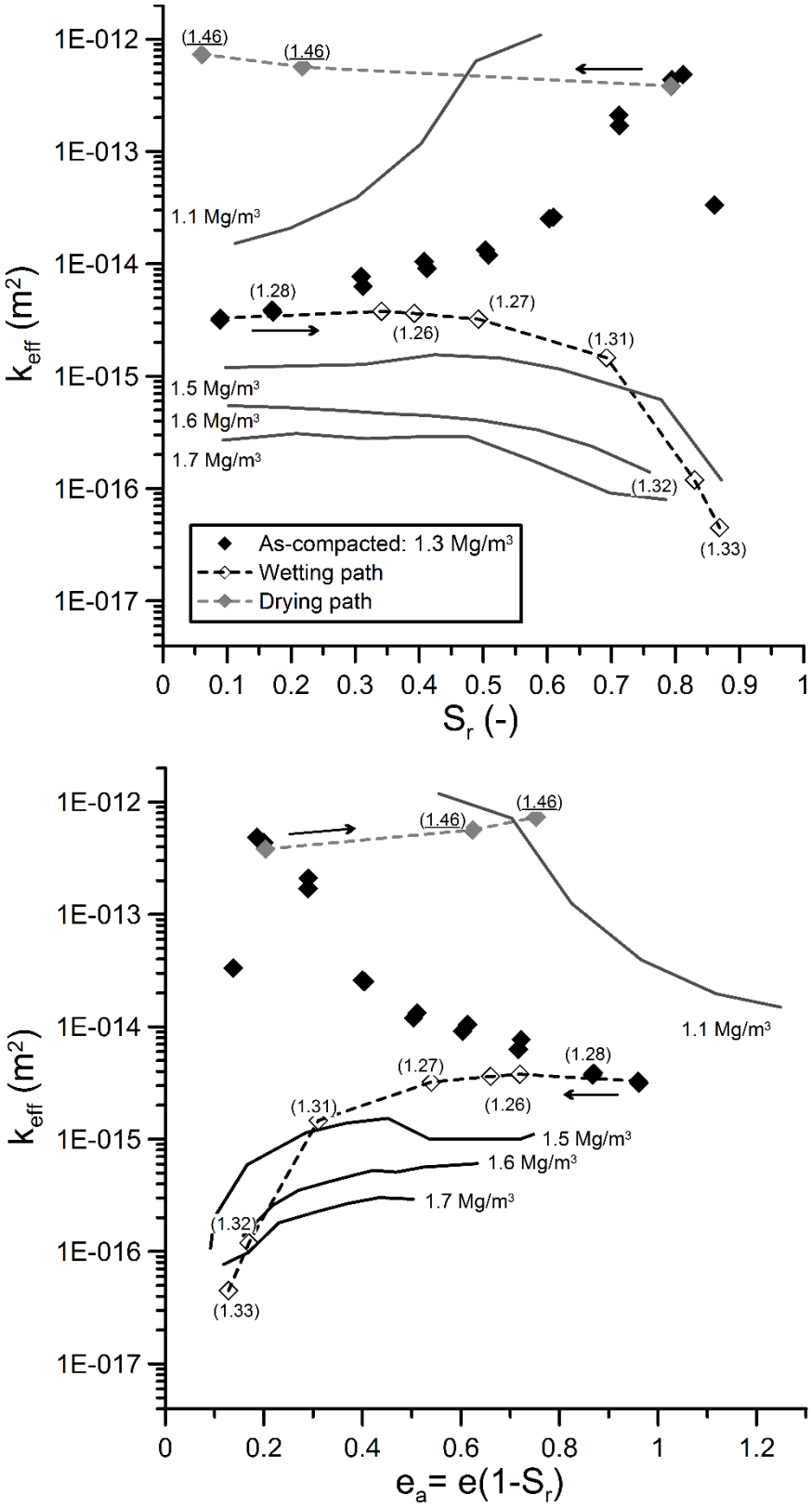

Figure 9. Evolution of k_{eff} with S_r and e_a during wetting and drying for specimens compacted to 1.3 Mg/m3

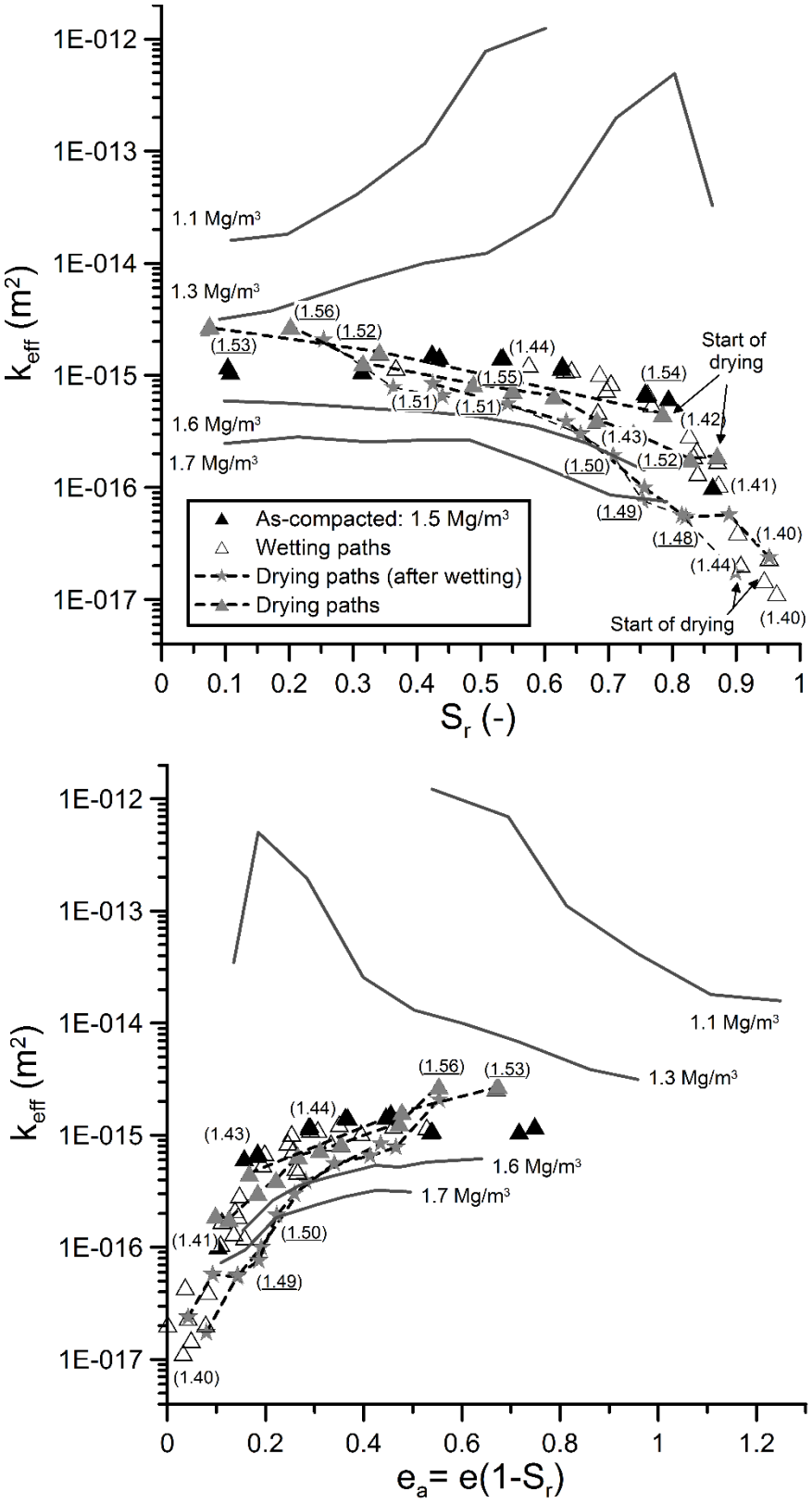

Figure 10. Evolution of k_{eff} with S_r and e_a during wetting and drying for specimens compacted to 1.5 Mg/m3

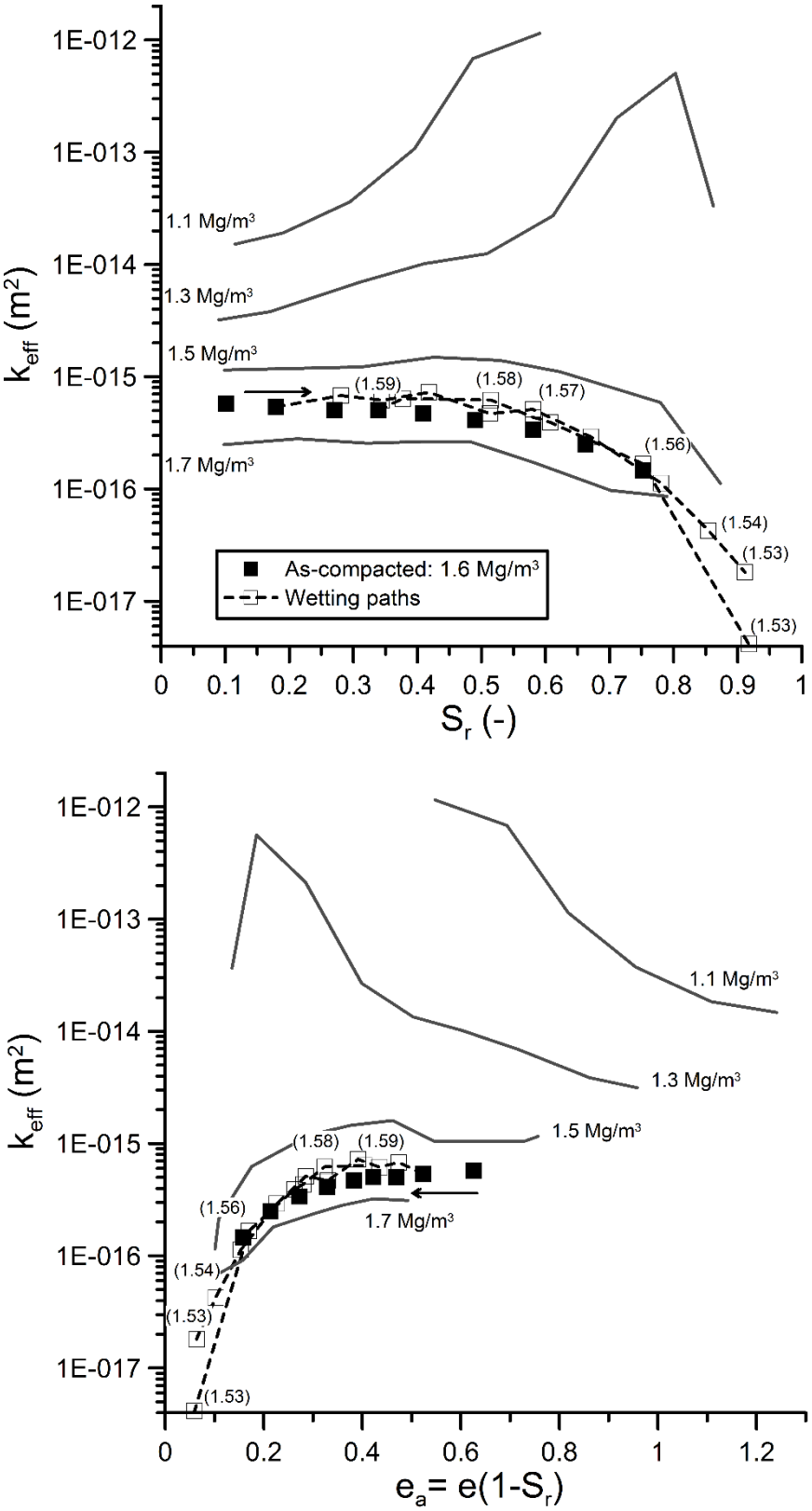

Figure 11. Evolution of k_{eff} with S_r and e_a during wetting and drying for specimens compacted to 1.6 Mg/m3

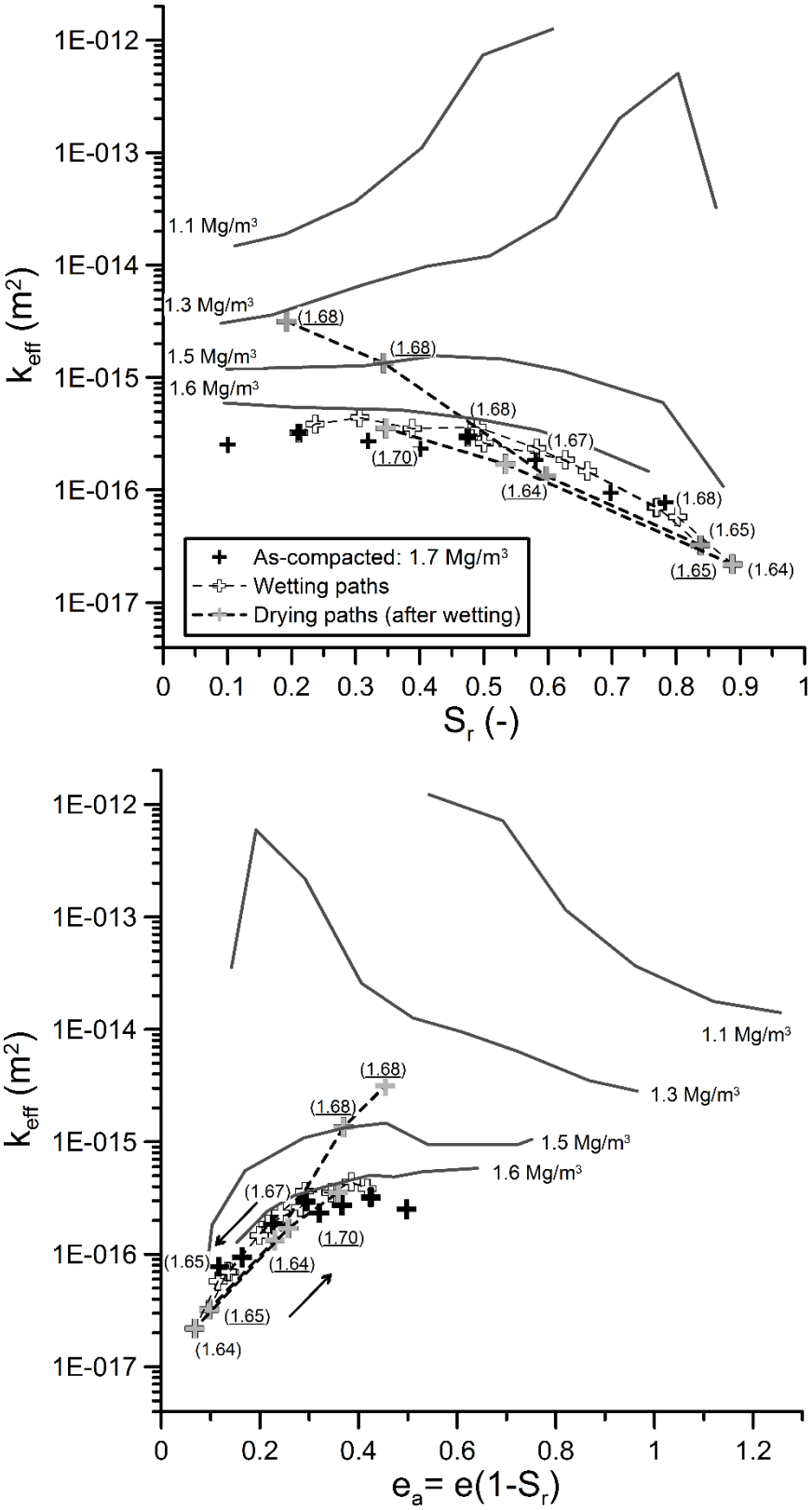

Figure 12. Evolution of k_{eff} with S_r and e_a during wetting and drying for specimens compacted to 1.7 Mg/m3

6. Microstructural study

Mercury intrusion porosimetry (MIP) tests were carried out to evaluate the pore size density (PSD) function of as-compacted specimens and samples subjected to wetting and drying paths (see Table 1). Figures 13-17 show the PSD curves for the five as-compacted dry densities tested in this study.

The PSD curves for specimens compacted to 1.1 Mg/m^3 (Figure 13) show a progressive evolution from mono-modal towards bi-modal density functions with increasing the as-compacted S_r. Bi-modal density functions are attributed here to the creation of clay aggregates during wetting that, in combination with the low compaction stresses required to achieve loose density states, allow the creation of an important proportion of macro pores. A dominant pore size between 1-3 μm may be observed for specimens with S_r < 40%. Specimens compacted to larger values of S_r > 40% show a PSD with two dominant peaks, one located around 0.15 μm (micro pores) and a second peak ranging between 3 – 300 μm (macro pores). Similar behaviour is observed in Figure 14 for specimens compacted to 1.3 Mg/m^3. In this case, the peak pore size for mono-modal PSD curves (S_r < 40%) decreases to 0.6 – 1.5 μm. Specimens with bi-modal PSDs display one peak at around 0.1 – 0.2 μm. Although the increase in dry density reduces the amount of large pores, its dominant pore size shows similar variation as in the loosest specimens. It can be noted that the increase in S_r seems responsible for the enhancement in the proportion of large pores (and its peak value) which in turn leads to increase k_{eff} in specimens compacted to 1.1 Mg/m^3 and 1.3 Mg/m^3. Nevertheless, the decrease in k_{eff} shown in Figure 9 for the specimen with S_r = 85% is explained by a decrease in its pore connectivity. The drastic reduction in the proportion of macro pores observed in Figure 14 for this specimen shows that the macro pores connectivity seems responsible for this behaviour.

Figure 15 presents the PSD curves for specimens compacted at 1.5 Mg/m^3. It is clear that pore sizes larger than 3.5 μm have minor impact on the effective air permeability irrespective of the as-compacted S_r. Dominance of a mono-modal PSD is observed for specimens with S_r < 60%. Larger values of S_r lead to a progressive increase in peak density and dominant pore size of micro pores. The proportion of macro pores also decreases with increasing S_r due to the high compaction stresses required to achieve denser states as well as the expansion of clay aggregates. Similar trends are observed for specimens compacted to 1.6 Mg/m^3 and 1.7 Mg/m^3 as observed in Figures 16 and 17. There, the increase in compaction density reduces the maximum pore size to 2 μm. From the inspection of Figures 15 - 17, S_r = 60% seems to define the transition between mono-modal and bi-modal PSDs. This is consistent with the threshold

value reported in Figures 6 and 7 where k_{eff} reduces with increasing S_r, caused by the reduction in the proportion of connected macro pores.

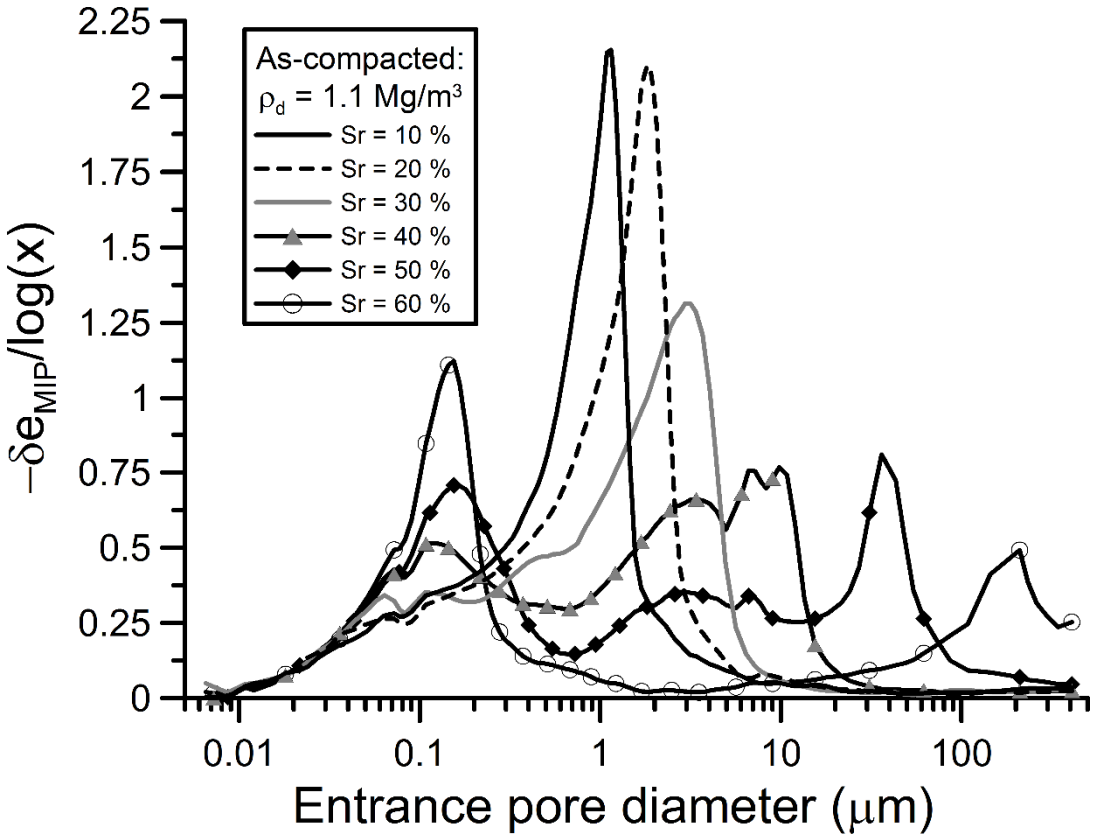

Figure 13. PSD curves for specimens compacted to 1.1 Mg/m3

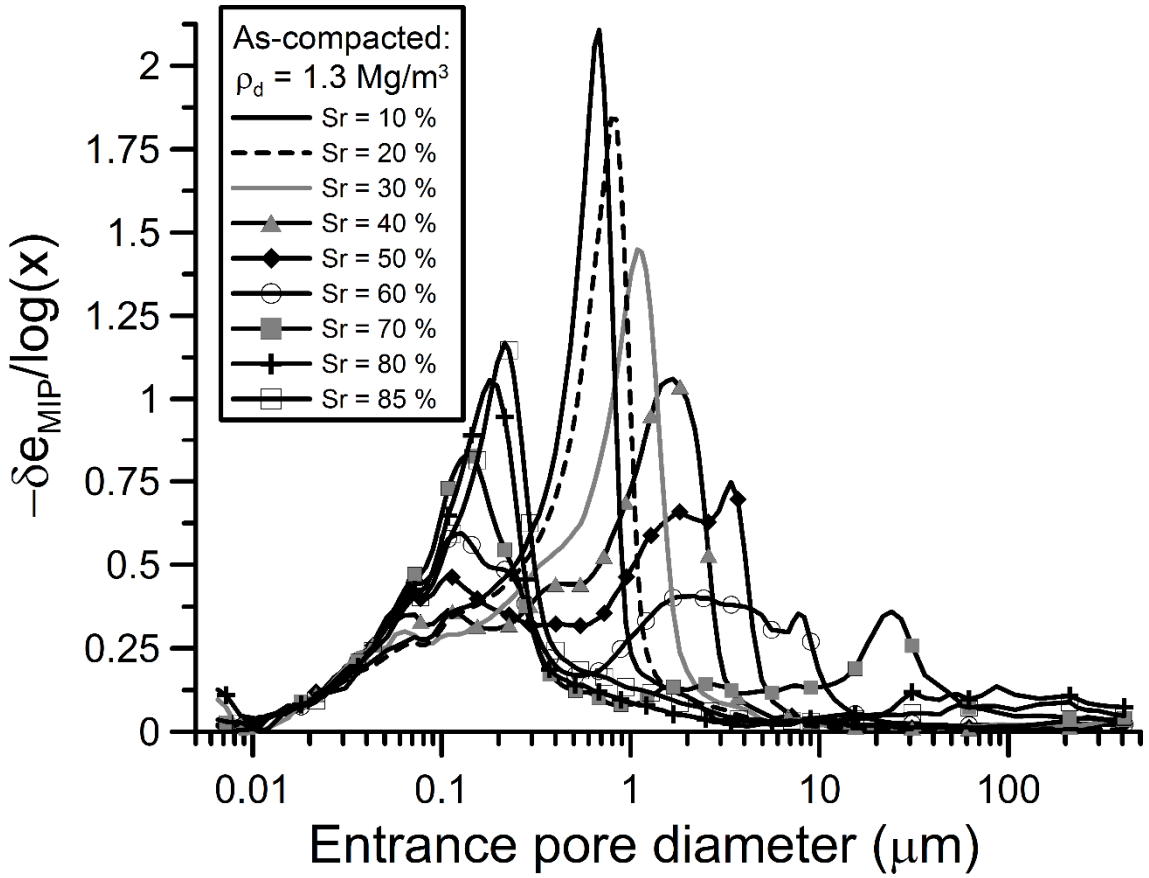

Figure 14. PSD curves for specimens compacted to 1.3 Mg/m3

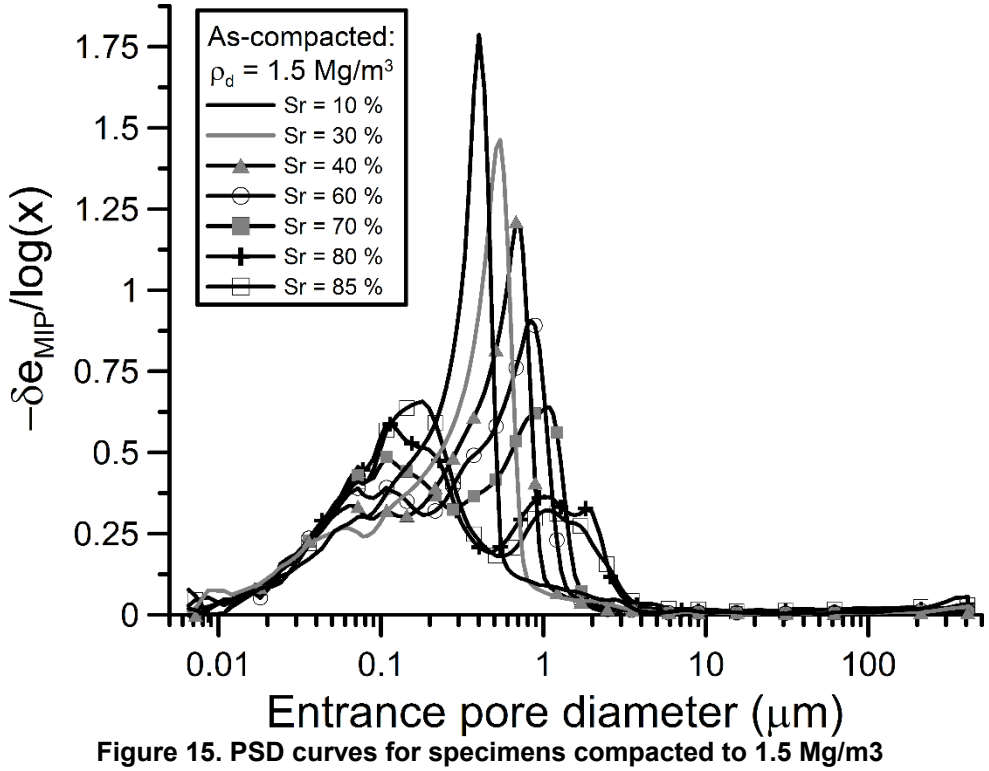

Figure 15. PSD curves for specimens compacted to 1.5 Mg/m3

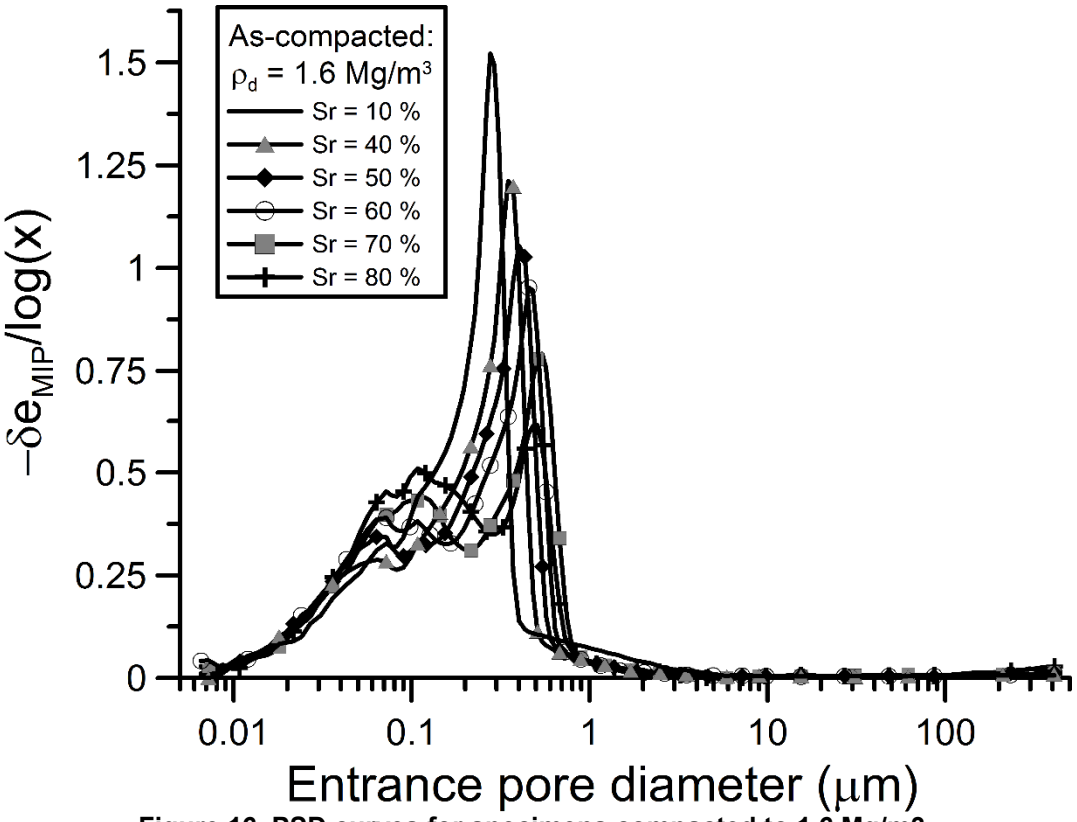

Figure 16. PSD curves for specimens compacted to 1.6 Mg/m3

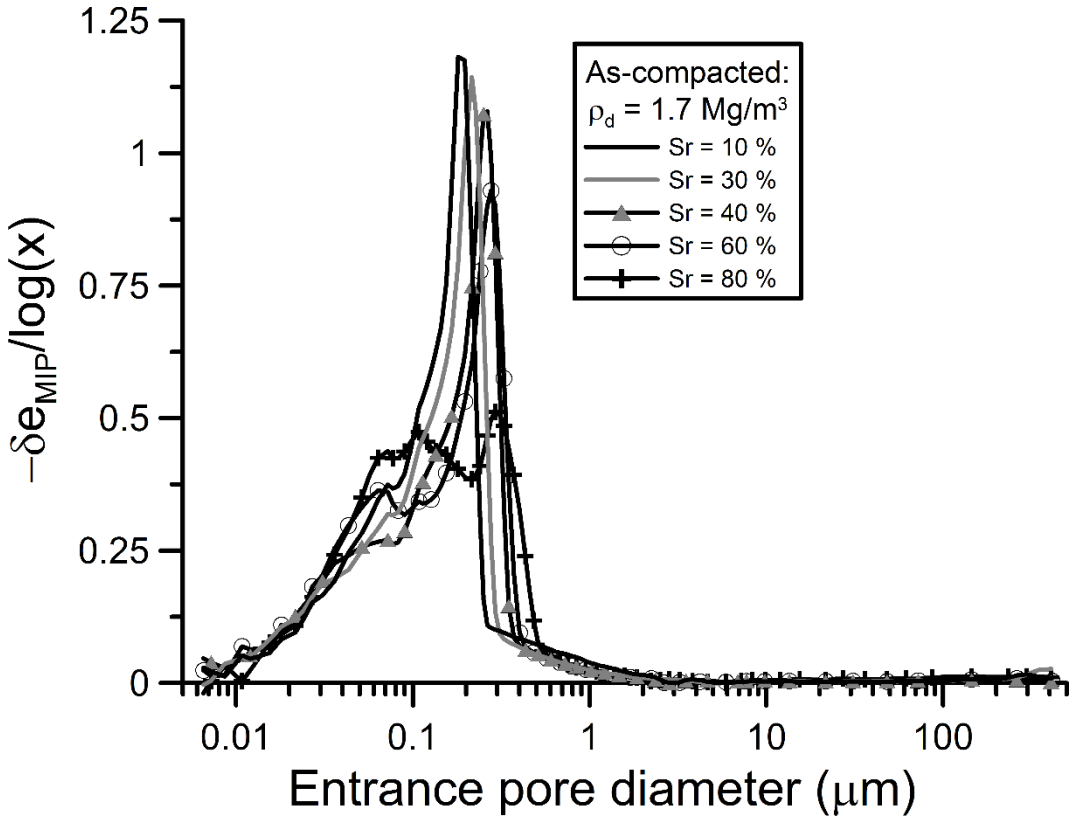

Figure 17. PSD curves for specimens compacted to 1.7 Mg/m3

The PSD curves for specimens compacted to 1.10 Mg/m^3, 1.30 Mg/m^3 and 1.50 Mg/m^3 that were subsequently exposed to controlled wetting and drying are presented in Figures 18, 19 and 20, respectively. Black solid lines represent the as-compacted state whereas dashed lines refer to the PSD curve obtained at the end of the applied hydraulic path. Initial and final conditions (ρ_d and S_r) are also indicated for clarity. Grey solid lines, which refer to PSD curves of as-compacted specimens with similar states as those achieved at the end of hydraulic paths, are included in these figures for comparison. In Figure 18, PSD curves for three specimens compacted to 1.10 Mg/m^3 and then subjected to wetting are shown. There is a clear influence of the as-compacted microstructure on the evolution of the PSD during wetting. The specimen compacted at S_r = 10% then wetted up to 65% seems to preserve its initially mono-modal nature. The increase in the dominant pore diameter observed in this specimen is associated here to the re-arrangement of the soil microstructure (i.e., local collapse as well as slippage between clay aggregates) due to the expansion of the soil aggregates upon wetting. It is interesting to note the formation of a bi-modal PSD for the specimen wetted to 75%. Although less evident, subtle indication of the formation of a bi-modal PSD upon wetting may also be appreciated for the specimen wetted up to 65 %. The bi-modal PSD of specimen compacted at S_r = 40% is still preserved after reaching 63%. However, there is evidence of the reduction in macro porosity, due to the expansion of the clay aggregates. Minor modifications in the PSD are observed for the dried specimen. There, small reduction in the proportion of macro and micro pores seems to be compensated by an increase in the number of pores with sizes between 1 -10 μm. It can be seen that PSDs obtained at the end of either wetting and drying paths are quite different from those curves for as-compacted specimens used here as a reference. Figure 19 shows the PSDs for samples compacted to 1.30 Mg/m^3 that were then wetted and dried. Wetting up to S_r = 65% shifts the mono-modal PSD curve and reduces its peak density and dominant pore size without changing the shape of the density function. The fact that the global dry density tended to increase during the wetting path is indicative of soil collapse. Shrinkage due to drying reduces the number of small pores whereas slightly increases the proportion of macro pores. Again, final PSD curves are not similar to those obtained in as-compacted samples at similar Sr.

The density function for dense specimens (1.5 Mg/m^3) after wetting and drying is presented in Figure 20. Two samples wetted to very similar S_r are reported in this figure. Minor modifications in the PSD are observed for the specimen originally compacted to low S_r. Its mono-modal density function is preserved even after reaching S_r = 90%. The specimen wetted from S_r = 60% shows a PSD that shifted to the left, with a lower dominant pore size and less proportion of macro pores, compared with the as-compacted state. Drying has minor impact on the PSD for the dense specimen. The reduction in the proportion of micro pores between 0.1-0.2 μm is

caused by the shrinkage of clay aggregates due to drying. On the other hand, the application of a wetting-drying cycle causes the movement of the PSD towards lower pore sizes as well as an increase in peak density. Microstructural changes caused by drying seems not be reversible on subsequent wetting.

Based on the MIP results described above, the following points deserve to be highlighted:

- The increase in k_{eff} with increasing S_r for specimens compacted to dry densities ≤ 1.30 Mg/m^3 is due to the creation of large macro pores as a consequence of clayey aggregation. These macro pores are preferential path for gas flow. The increase in S_r beyond 80% seems to produce the reverse effect, i.e., a decrease in the proportion of macro pores and therefore a reduction in k_{eff}.
- For dry densities ≥ 1.5 Mg/m^3, the small variation in k_{eff} for specimens compacted to S_r < 60% is in agreement with the minor modifications in their dominant mono-modal PSDs. For S_r > 60%, the increase in the amount of micro pores and a reduction in macro porosity, are responsible for the marked reduction in k_{eff} observed in Figures 6 and 7. This behaviour tends to modify the density function towards bi-modal type PSDs with dominance of the micro porosity.
- Regarding to specimens wetted and dried, the evolution of the PSD is strongly dependent on the “as-compacted microstructure”. PSDs obtained at the end of wetting or drying paths are clearly different compared with density functions for as-compacted specimens at similar S_r. This behaviour is in line with the differences in k_{eff} observed between as-compacted samples and those subjected to hydraulic paths. Despite the small changes in the PSD observed for dried specimens, the micro-macro interaction that occurred during shrinkage leads to increase k_{eff}, due to the enhancement of the macro (even meso) porosity.

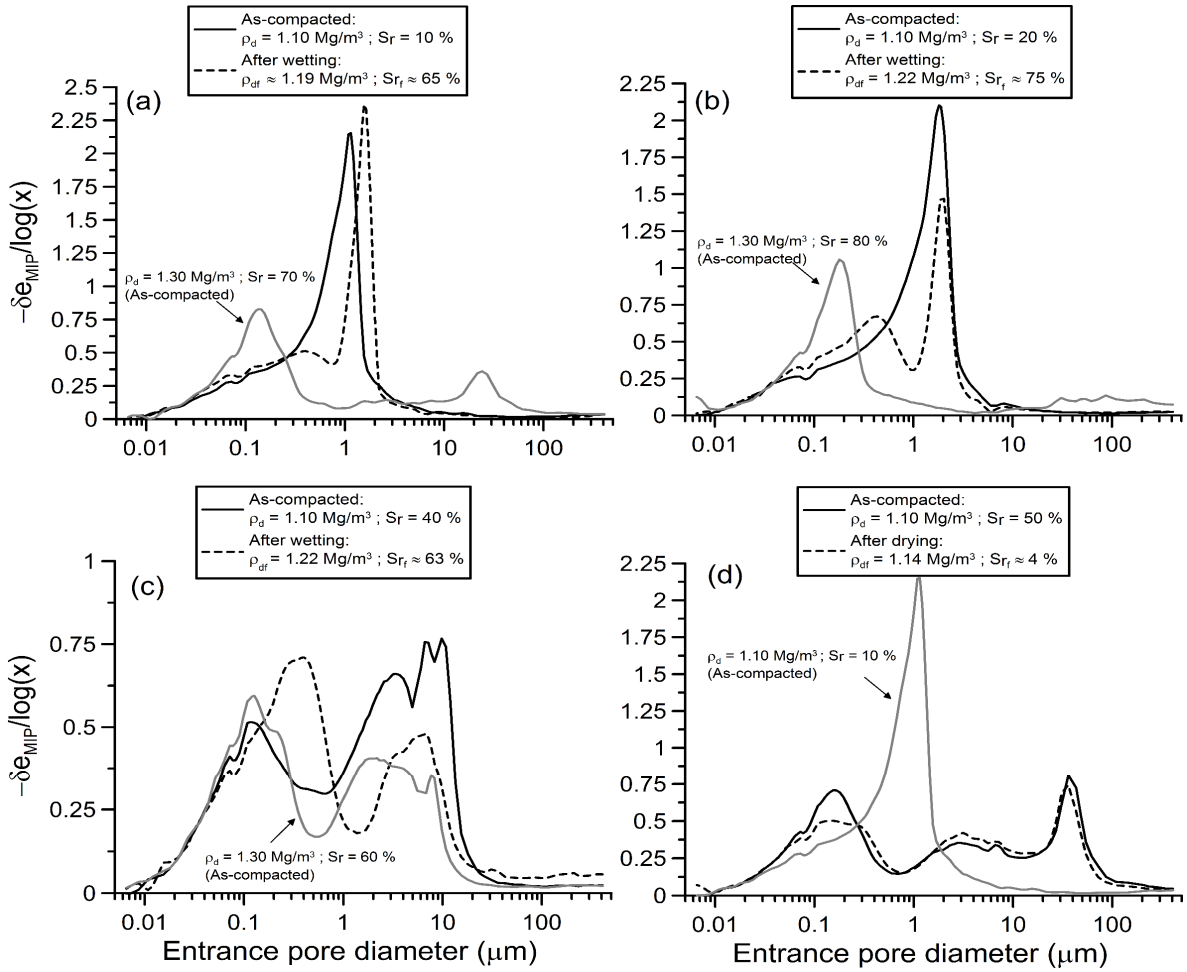

Figure 18. Evolution of the PSD for wetted and dried specimens compacted to 1.1 Mg/m3

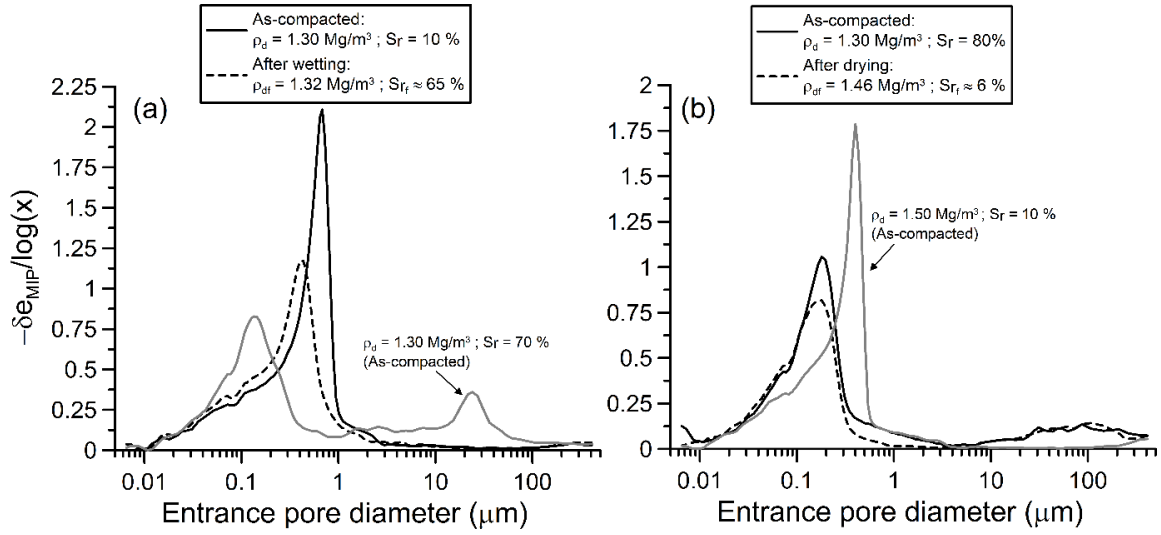

Figure 19. Evolution of the PSD for wetted and dried specimens compacted to 1.3 Mg/m3

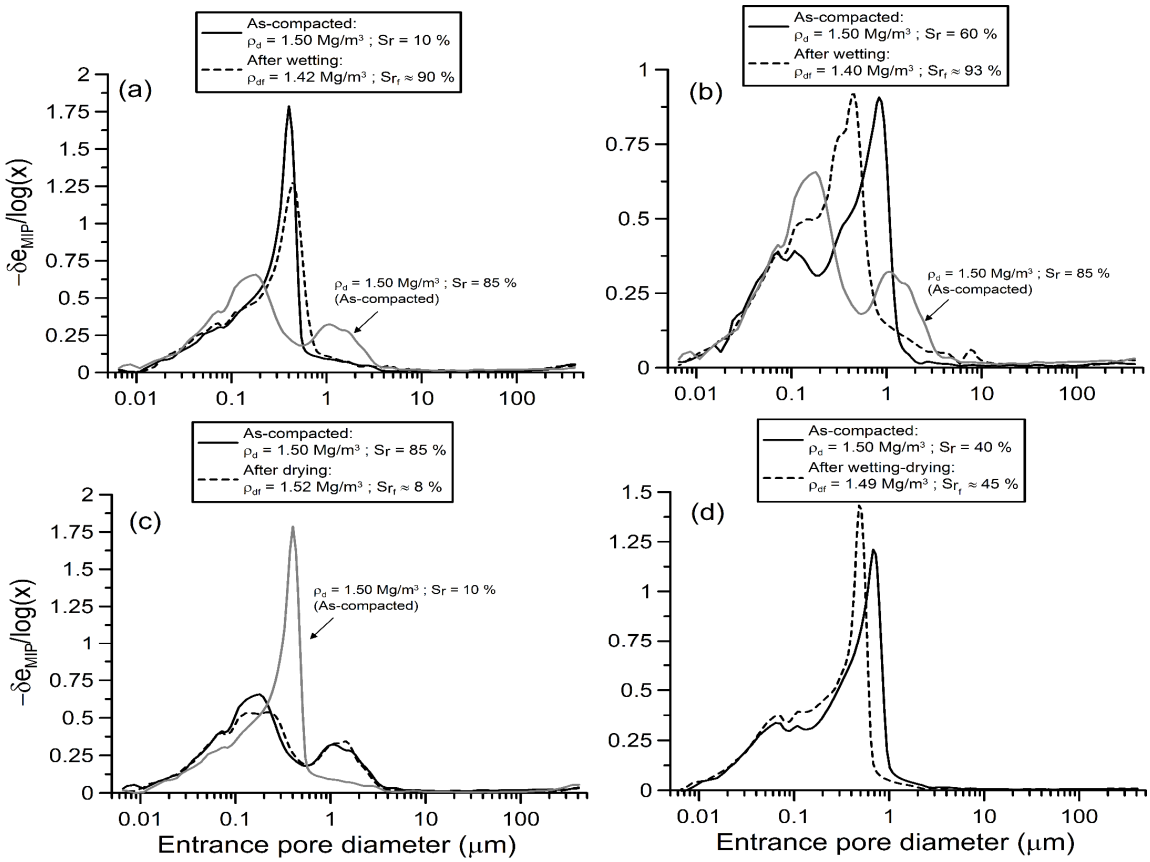

Figure 20. Evolution of the PSD for wetted and dried specimens compacted to 1.5 Mg/m3

A first attempt has been made here to link effective air permeability and microstructural parameters obtained from MIP data. To do so, the approach by Delage and Lefebvre (1984) was adopted to estimate the delimiting pore size, x_{del}, which separates micro and macro porosities. Figure 21 shows the variation of x_{del} with S_r for as-compacted specimens. Two trends are observed in this figure depending on S_r. For S_r < 75%, which is similar to the S_r at optimum, x_{del} varies nonlinearly with S_r and ρ_d. For a given density, maximum values of x_{del} are observed in loose specimens between 20 < S_r < 30%. This peak decreases with increasing the compaction density. The delimiting pore size, x_{del}, shows a narrow variation around 0.2 μm for Sr > 75%. The inspection of Figures 13-17, however, suggest that macro pores are significantly larger than those values in Figure 21 estimated according to Delage and Lefebvre (1984), at least for compaction densities lower than 1.5 Mg/m^3. Although it is not presented in this paper, the comparison between k_{eff} with the macro void ratio (e_M) estimated from MIP data using Figure 21, show very poor correlation for loose specimens (≤1.3 Mg/m^3). This result indicates that a different approach is required to link macroscopic results with microstructural data obtained from MIP results.

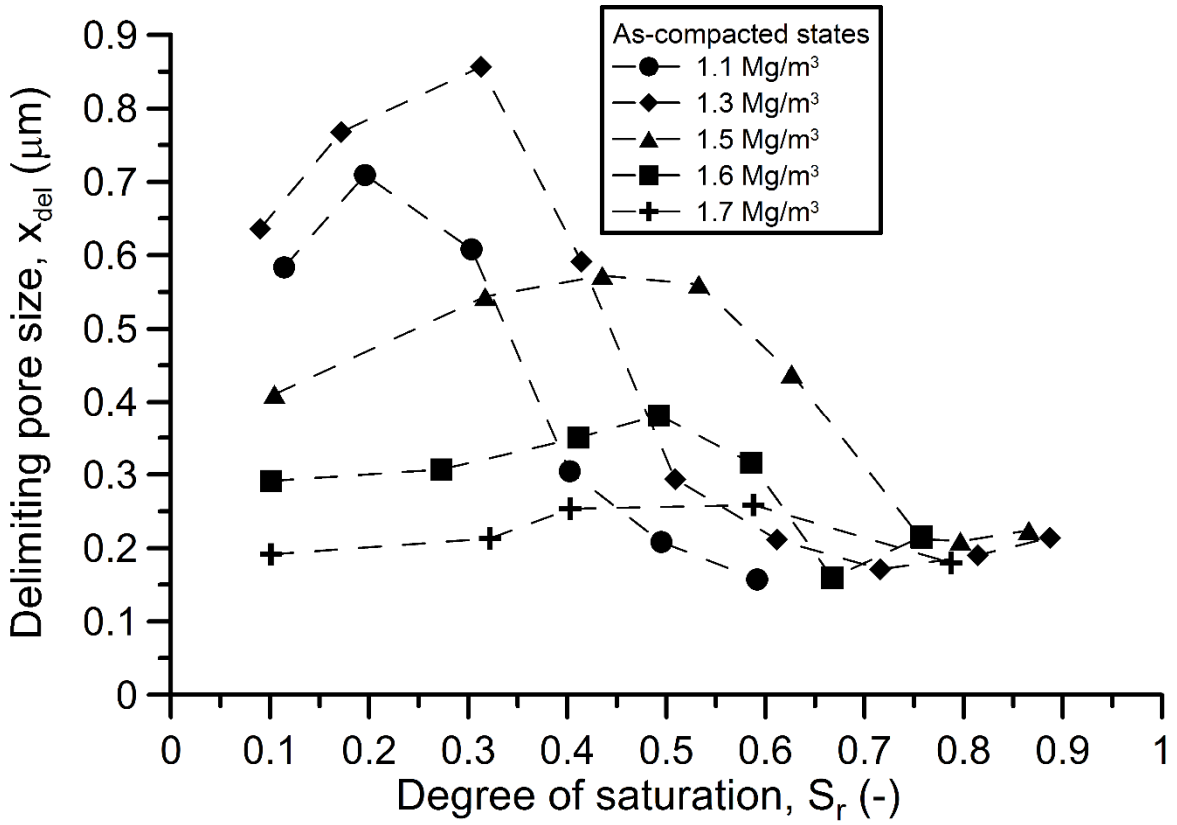

Figure 21.Delimiting pore size for as-compacted states estimated from MIP tests as in Delage & Lefebvre (1984)

7. Alternative interpretation

When liquid water is mixed with dry soil, saturated clay particles merge each other to create clay aggregates. However, the interaction between clay aggregates during compaction and subsequent wetting/drying paths produce a network of highly connected pores that are filled by water and air. Macroscopic measurements of k_{eff} in combination with microstructural data presented above have shown that the gas flow through compacted clay is strongly influenced by the proportion of macro pores which have high connectivity. In Figure 22, the dominant macro pore diameter (i.e. the peak for the larger pores observed in each PSD shown above) is plotted against the as-compacted S_r. Two trends are observed in this figure. Dense specimens (≥1.5 Mg/m^3) show a dominant macro-pore diameter lower than 1μm, irrespective of the as-compacted Sr. Dominant macro pores from 0.8 μm up to 300 μm are created by compaction in loose specimens (<1.3 Mg/m^3) which are consistent with their high k_{eff} (see Figure 6). The grey solid line included in this figure indicates the transition between mono-modal and bi-modal PSD as a function of the as-compacted S_r. Clearly, the increase in S_r tends to create large macro pores, whose proportion is controlled by the as-compacted density. Figure 22 support the hypothesis that highly connected porosity, which controls the gas flow, is mainly composed by large macro pores. Therefore, changes in the low connected porosity,

due to swelling/shrinkage of clay aggregates, only affect k_{eff} through modifications in large pores connectivity.

Based on the above, two levels of porosity are adopted here to represent the microstructure of the compacted soil (see Figure 23(a)): (i) highly connected porosity, and (ii) low connected porosity. Separation between these two levels is given by a delimiting pore size, x_{del}, defined here by considering the frequency distribution, f(di), as well as the estimated degree of saturation, both obtained from the MIP tests. The degree of saturation estimated from MIP data is defined as $S_r = 1 - S_{rnw}$, where S_{rnw} stands for the nonwetting mercury degree of saturation (Romero et al., 1999). Figure 23(b) describes the definition of x_{del} using the MIP data obtained for a specimen compacted to 1.3 Mg/m^3 and S_r = 80%. It is assumed that liquid water fills small pores first, i.e. the low connected gas porosity. Pores sizes larger than x_{del} conform the highly connected gas porosity which controls the gas flow.

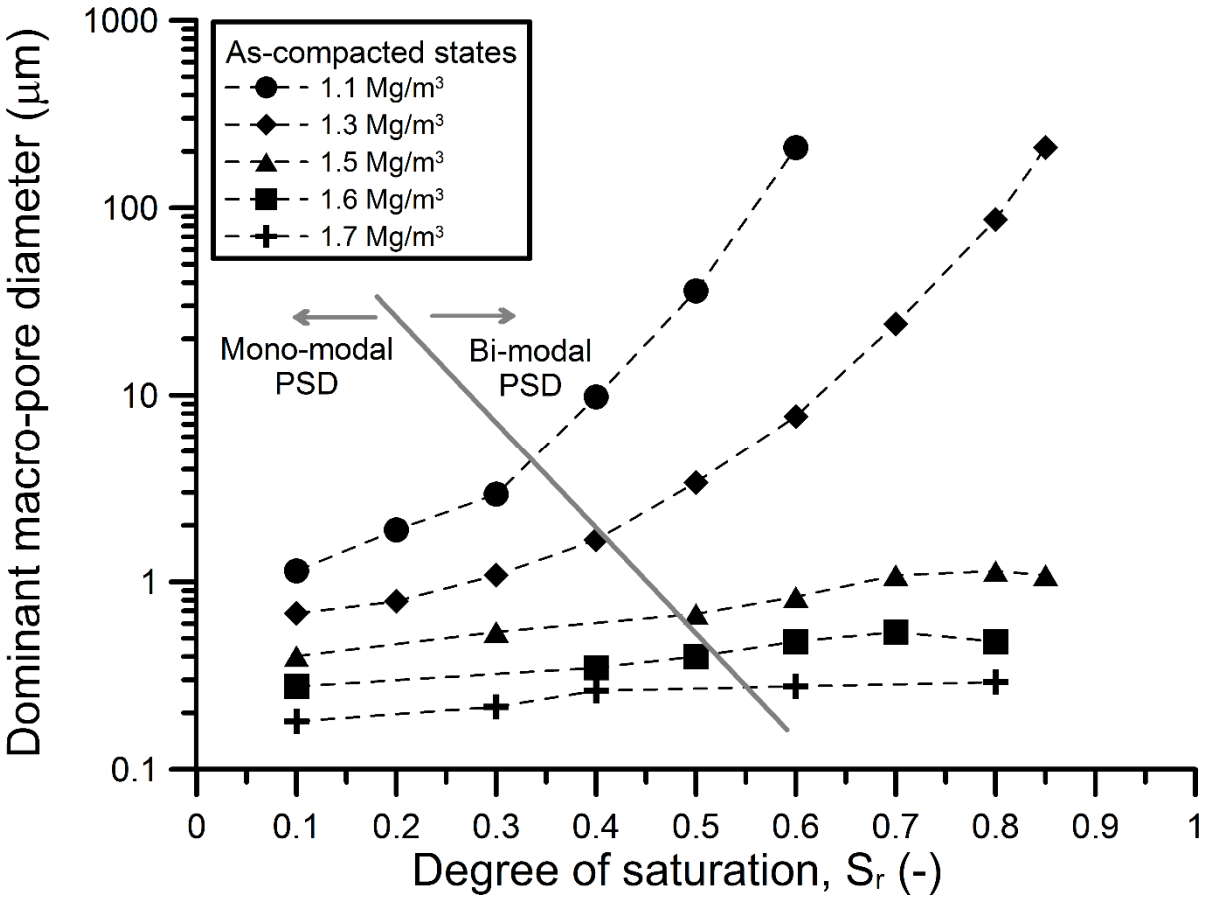

Figure 22.Variation of the dominant macro-pore diameter with the as-compacted S_r.

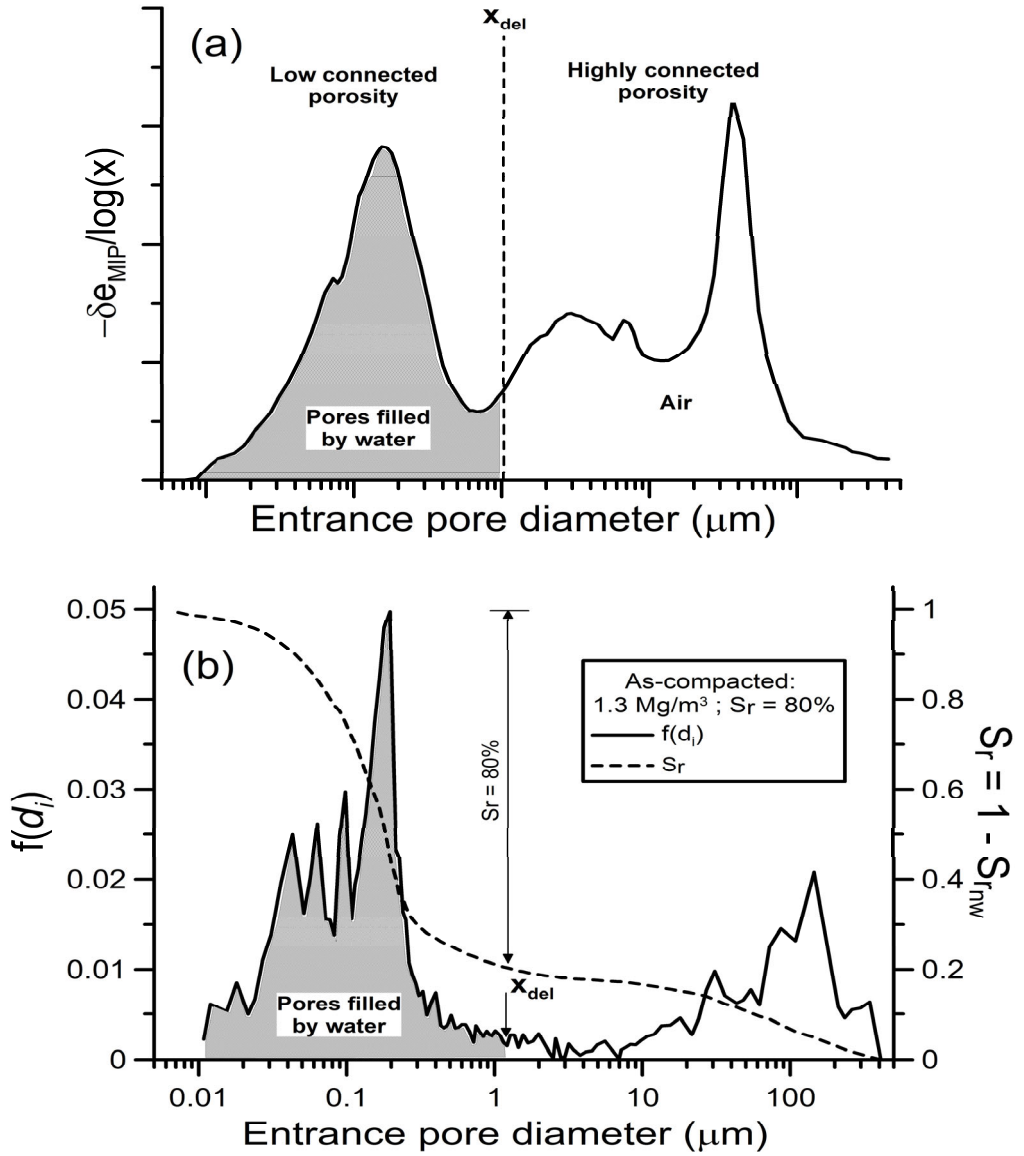

Figure 23.(a) Schematic representation of highly connected and low connected porosities in compacted clay. (b) Estimation of the delimiting pore size (x_{del}).

García-Bengoechea et al. (1979) derived an expression to estimate the saturated permeability of silty clays from pore size distribution data. It takes the form:

$$k = C_s.PSP \quad (4)$$

where Cs is a shape factor that depends on the geometry of the pores and PSP is the pore size parameter which incorporates information about the soil microstructure. The PSP is defined as:

$$PSP = E(r^2).n = \sum_{i=r_{min}}^{r_{max}} f(r_i).r_i^2.n \quad (5)$$

where n is the porosity of the soil and r is the radius of the pore. $E(r^2)$ is defined as the product of the frequency distribution times the radius squared. The exponent in the latest comes from the adoption of the Hagen-Poiseuille equation for laminar flow through a cylindrical pipe.

In this study, $E(r^{\alpha})$ rather than $E(r^2)$ is adopted in order to explore, in a simple way, other possibilities for gas flow through capillary tubes of cylindrical shape. $E(r^{\alpha})$ is therefore defined as:

$$E(r^{\alpha}) = \sum_{r_{delimiting}}^{r_{max}} f(r_i).r_i^{\alpha} \quad (6)$$

where α is now a parameter.

Figure 24 shows the variation of the regression coefficient, R^2, for different values of parameter α, estimated by a fitting process using 32 MIP data sets obtained for as-compacted specimens. The regression coefficient shows a maximum value equal to 0.94 for $\alpha \approx 0.50$. It can be seen that for α = 2, which correspond to the Hagen-Poiseuille equation adopted in the original derivation by García-Bengoechea et al. (1979), the estimated R^2 is quite low. This result suggest that Eq. 5, which defines the pore size parameters, could be written in a general form by replacing the function $E(r^2)$ by $E(r^{\alpha})$, which could be seemed as a connectivity factor in which the value of the exponent, for air flow through compacted clay seems to be closed to 0.5 (rather than 2 as in the Hagen-Poiseuille equation).

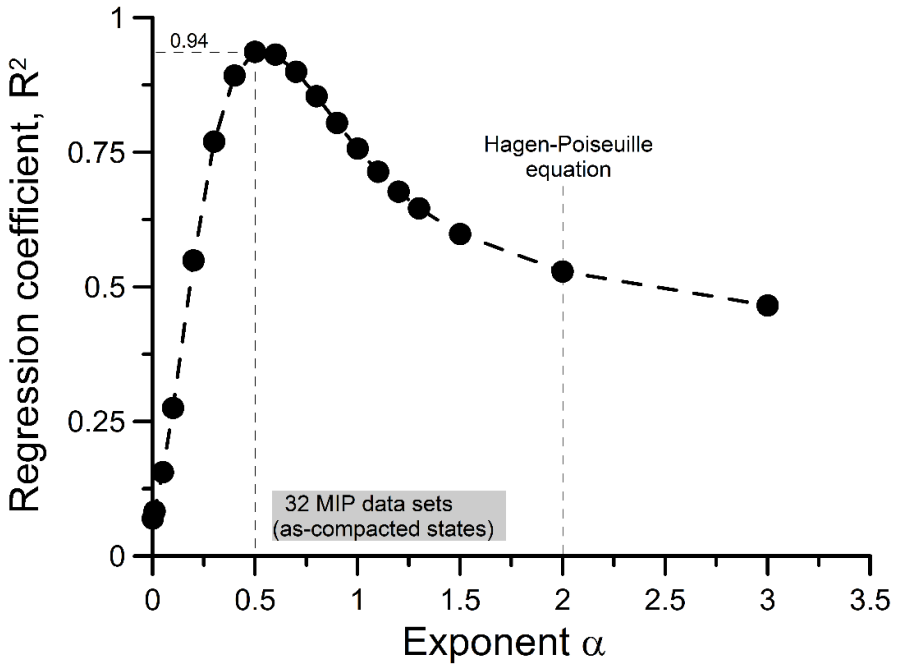

Figure 24.Best fitting for exponent a using 32 MIP data sets (as-compacted specimens).

The result shown in Figure 24 may be justified by adopting the Darcy-Weisbach equation, instead of the Hagen-Poiseuille equation, for the derivation of the permeability function. This phenomenological equation has been successfully employed to represent the fluid flow in circular pipes including the pressure drop in air conducts (ventilation systems) (e.g., Brown,

2002). The general expression for the Darcy-Weisbach equation of a pressure drop, Δp, is given by:

$$\Delta p = f \cdot \frac{L\rho}{2} \cdot \frac{v^2}{D} \quad (7)$$

where Δp is the pressure drop, f is the friction factor, D is the diameter of the pipe, *v* is the mean flow velocity and ρ is the density of the fluid. As in the Hagen-Poiseuille equation adopted by García-Bengoechea et al., Eq. 7 assumes incompressible fluid. However, the Darcy-Weisbach equation has been employed with success for predicting the head loss in gas pipes of circular shape where the change in density due to a pressure drop is small, such as in air ventilation systems (Swamee and Jain, 1976; Brown, 2002). In the tests described above, the maximum pressure loss applied during the air injection stage was equal to 40kPa. Nevertheless, only the initial 50% drop in air pressure was considered in the estimation of k_{eff}. It means Δp_{air}=20 kPa which corresponds, according to the ideal gas low, and assuming isothermal conditions, to an average variation in gas density of $\Delta\rho \approx \pm 0.12$ kg/m^3. Such a small variation justifies, in this case, the adoption of the Darcy-Weisbach equation by assuming nearly incompressible fluid. After following the procedure described by García-Bengoechea et al. (1979), using the Darcy-Weisbach equation, the following expression for soil permeability is obtained (full derivation is given in the Appendix):

$$k = 2 \cdot \sqrt{\frac{L}{\Delta P \rho f}} \cdot \mu_a \cdot n \cdot \sum_{i=r_{min}}^{r_{max}} f(r_i) \cdot \sqrt{r_i} \quad (8)$$

where μ_a is the viscosity of the fluid [kg/m.s], n is the porosity whereas f, ρ, Δp, and r_i stand as in Eq. 7. It can be noted that the exponent α defined by Eq. 6 is now equal to 0.5, the same value that provides the best estimate for the 32 MIP data sets previously shown in Figure 23. The PSP is now calculated as:

$$PSP = E(r^{0.5}).n = \sum_{i=r_{min}}^{r_{max}} f(r_i).r_i^{0.5}.n \quad (9)$$

Figure 25(a) compares k_{eff} with PSP estimated using Eq. 9. A linear relationship (in log scale) is observed for the 32 MIP data sets obtained from as-compacted specimens. The regression coefficient obtained using the Darcy-Weisbach equation is 0.94, as observed in Figure 24. Values of k_{eff} and PSP for specimens exposed to wetting and drying paths are included in Figure 25(b). The proposal presented here seems capable of representing the variation of k_{eff} with PSP for kaolin specimens compacted to a wide range of densities and water contents including soil states obtained after the application of hydraulic paths. Although only kaolin

samples were tested in this study, the approach presented here seems an alternative tool for studying the hydraulic behaviour of compacted soils in general.

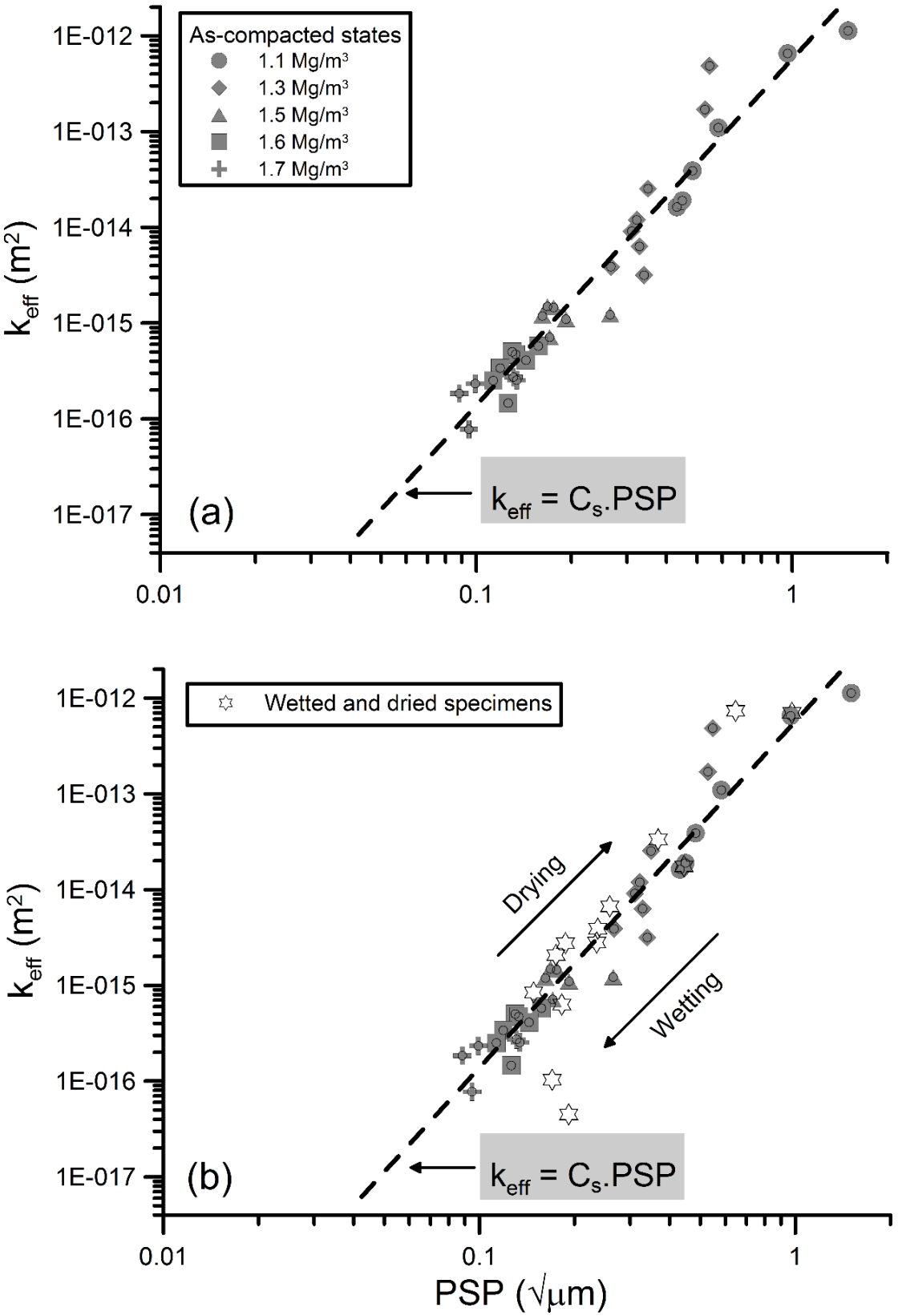

Figure 25. Relationship between k_{eff} and PSP. (a) As-compacted samples. (b) Wetted and dried specimens.

8. Concluding remarks

The influence of soil microstructure on air permeability in compacted clay has been evaluated in this paper. Detailed mapping of the effective air permeability for a wide range of densities and water contents was presented. Experimental results show that effective air permeability is mainly controlled by large pores that display high connectivity. An important variation in the pore size density function with the as-compacted density and degree of saturation was clearly demonstrated. Mono-modal PSDs were typically obtained for specimens compacted to low degrees of saturation, irrespective of the as-compacted dry density. An evolution towards bi-modal curves with increasing S_r (as-compacted states) was also observed. PDS curves for specimens subjected to wetting and drying paths showed strong influence of the as-compacted microstructure, which was consistent with the measured effective air permeability. The degree of saturation plays a double role on soil microstructure which, in turn, affects the effective air permeability: (i) reducing macro porosity due to the expansion of the clay aggregates, thus reducing k_{eff}, and (ii) enhancing the proportion of macro pores by modifying the PSD. An attempt was made in this paper to combine such a wider spectrum of permeabilities and initial soil microstructures into a unified approach using the pore size distribution obtained from MIP tests. To do so, two porosity levels were defined in terms of their connectivity. The separation between these levels of porosity is defined in terms of the global degree of saturation. It is assumed that liquid water fills first the micro pores which means that highly connected macro pores control the gas flow in compacted clay. A pore size parameter has been proposed which shows high correlation with the measured effective air permeability even for specimens subjected to wetting and drying paths. This led to the modification of the original proposal by García-Bengoechea et al. (1979) by defining a connectivity factor (Eq. 5) that account, for instance, for variations in the pore diameter along connected pores. Interestingly, the adoption of α=0.50 in Eq. 6 is consistent with the assumption that gas flow can be modelled according to the Darcy-Weisbach equation for predicting the head loss in gas pipes of circular shape, by assuming nearly incompressible fluid. Although further verification is required, the proposed model may be useful for modelling the gas flow through compacted geomaterials where the clayey fraction is dominant.

Acknowledgements

The research work presented in this paper was funded through an ARC Discovery Project *DP150103396 "Mechanics of hard soils and soft rocks"*. Authors are very grateful to the Australian Research Council for this support.

Table 1. Compaction states

Specimen ID	w	ρ_d	S_r	σ_{comp}	MIP test
	(-)	(Mg/m^3)	(-)	(kPa)	
1.1-10-1	0.06	1.08	0.12	353	After wetting
1.1-10-2	0.06	1.08	0.12	342	As-compacted
1.1-20-1	0.11	1.10	0.20	374	As-compacted
1.1-20-2	0.11	1.10	0.20	373	After wetting
1.1-30-1	0.16	1.10	0.31	335	As-compacted
1.1-30-2	0.16	1.10	0.31	330	
1.1-40-1	0.21	1.10	0.40	252	As-compacted
1.1-40-2	0.21	1.10	0.40	248	After wetting
1.1-50-1	0.26	1.09	0.49	177	As-compacted
1.1-50-2	0.26	1.09	0.49	173	
1.1-50-3	0.25	1.10	0.48		After drying
1.1-60-1	0.31	1.10	0.58	67	As-compacted
1.1-60-2	0.31	1.10	0.58	64	
1.3-10-1	0.038	1.27	0.094	1197	As-compacted
1.3-10-2	0.038	1.27	0.094	1204	After wetting
1.3-20-1	0.073	1.27	0.179	1132	As-compacted
1.3-20-2	0.073	1.27	0.179	1125	
1.3-30-1	0.126	1.28	0.312	1027	As-compacted
1.3-30-2	0.126	1.28	0.313	1005	
1.3-40-1	0.164	1.28	0.410	864	As-compacted
1.3-40-2	0.164	1.28	0.409	862	
1.3-50-1	0.202	1.28	0.504	663	As-compacted
1.3-50-2	0.202	1.28	0.504	649	
1.3-60-1	0.240	1.29	0.604	499	As-compacted
1.3-60-2	0.240	1.28	0.603	495	
1.3-70-1	0.277	1.29	0.699	296	As-compacted
1.3-70-2	0.277	1.29	0.699	295	
1.3-80-1	0.310	1.29	0.786	190	As-compacted
1.3-80-2	0.310	1.29	0.789	183	After drying
1.3-80-3	0.308	1.28	0.773		
1.3-85-1	0.328	1.30	0.846		As-compacted
1.3-90-1	0.342	1.30	0.883		
1.5-10-1	0.034	1.43	0.107	4005	As-compacted
1.5-10-2	0.034	1.46	0.112	4745	After wetting
1.5-30-1	0.096	1.47	0.319	3839	As-compacted
1.5-30-2	0.096	1.47	0.320	3812	After wetting+drying
1.5-50-1	0.134	1.46	0.440	3056	As-compacted
1.5-50-2	0.134	1.46	0.439	2801	After wetting+drying
1.5-60-1	0.161	1.46	0.532	2666	As-compacted
1.5-60-2	0.161	1.47	0.535	2615	
1.5-70-1	0.188	1.47	0.624	2161	As-compacted
1.5-70-2	0.188	1.47	0.624	2124	After wetting
1.5-80-1	0.223	1.47	0.746	1523	
1.5-80-2	0.223	1.47	0.748	1508	As-compacted
1.5-85-1	0.234	1.48	0.791		After drying

1.5-85-2	0.234	1.48	0.791		As-compacted
1.5-90-1	0.254	1.49	0.866		After drying
1.5-90-2	0.254	1.49	0.866		As-compacted
1.6-10-1	0.027	1.55	0.102	9165	As-compacted
1.6-15-1	0.045	1.60	0.183	9602	After wetting
1.6-20-1	0.067	1.60	0.274	9348	As-compacted
1.6-30-1	0.083	1.60	0.343	7597	After wetting
1.6-40-2	0.103	1.59	0.416	7886	As-compacted
1.6-50-1	0.123	1.60	0.497	7017	As-compacted
1.6-60-1	0.146	1.60	0.592	6421	As-compacted
1.6-70-2	0.162	1.60	0.662	5104	As-compacted
1.6-80-1	0.185	1.60	0.752	5233	As-compacted
1.7-10-1	0.027	1.70	0.131	21102	As-compacted
1.7-20-1	0.045	1.71	0.217	17910	After wetting+drying
1.7-30-1	0.067	1.70	0.324	18079	As-compacted
1.7-40-1	0.083	1.71	0.410	14420	As-compacted
1.7-50-2	0.103	1.69	0.486	13923	After wetting
1.7-60-1	0.123	1.70	0.590	13194	As-compacted
1.7-70-1	0.146	1.69	0.687	11936	After wetting + drying
1.7-80-2	0.162	1.70	0.784	10108	As-compacted

Table 2. Effective air permeability and pore size parameter for as-compacted states.

Specimen ID	S_r	e_a	k_{eff}	PSP	Comment
	(-)	(-)	(m^2)	(-)	
1.1-10-1	0.117	1.239	1.52E-14		Wetted (see Table 3)
1.1-10-2	0.113	1.250	1.63E-14	0.4324	
1.1-20-1	0.195	1.113	1.90E-14	0.4494	
1.1-20-2	0.192	1.114	2.07E-14		Wetted (see Table 3)
1.1-30-1	0.302	0.958	3.89E-14	0.4843	
1.1-30-2	0.300	0.965	3.65E-14		Wetted (see Table 3)
1.1-40-1	0.401	0.821	1.10E-13	0.5848	
1.1-40-2	0.401	0.818	1.25E-13		Wetted (see Table 3)
1.1-50-1	0.493	0.700	6.53E-13	0.9683	
1.1-50-2	0.494	0.697	6.40E-13		
1.1-50-3	0.485	0.701	6.71E-13		Dried (see Table 3)
1.1-60-1	0.584	0.563	1.13E-12	1.5098	
1.1-60-2	0.600	0.530	1.04E-12		
1.3-10-1	0.089	0.961	3.16E-15	0.3419	
1.3-10-2	0.089	0.960	3.29E-15		Wetted (see Table 3)
1.3-20-1	0.170	0.869	3.89E-15	0.2678	
1.3-20-2	0.172	0.867	3.72E-15		
1.3-30-1	0.312	0.716	6.32E-15	0.3286	
1.3-30-2	0.309	0.722	7.71E-15		
1.3-40-1	0.412	0.603	9.11E-15	0.3113	
1.3-40-2	0.408	0.613	1.05E-14		
1.3-50-1	0.508	0.504	1.19E-14	0.3221	
1.3-50-2	0.503	0.511	1.33E-14		

1.3-60-1	0.603	0.404	2.53E-14	0.3518	
1.3-60-2	0.609	0.400	2.60E-14		
1.3-70-1	0.712	0.289	1.70E-13	0.5298	
1.3-70-2	0.712	0.290	2.10E-13		
1.3-80-1	0.812	0.186	4.85E-13	0.5481	
1.3-80-2	0.793	0.203	3.82E-13		Dried (see Table 3)
1.3-80-3	0.795	0.200	4.35E-13		
1.3-85-1	0.861	0.138	3.34E-14	0.3737	
1.3-90-1	0.895	0.104			
1.5-10-1	0.104	0.748	1.22E-15	0.2663	
1.5-10-2	0.108	0.716	1.09E-15		Wetted (see Table 3)
1.5-30-1	0.315	0.537	1.10E-15	0.1928	
1.5-30-2	0.314	0.539	1.11E-15		Wetted+dried (see Table 3)
1.5-50-1	0.435	0.445	1.49E-15	0.1678	
1.5-50-2	0.424	0.455	1.59E-15		Wetted+dried (see Table 3)
1.5-60-1	0.531	0.368	1.46E-15	0.1759	
1.5-60-2	0.535	0.363	1.48E-15		Wetted (see Table 3)
1.5-70-1	0.627	0.289	1.19E-15	0.1618	
1.5-70-2	0.628	0.290	1.25E-15		Wetted (see Table 3)
1.5-80-1	0.760	0.182	6.82E-16		
1.5-80-2	0.758	0.184	7.13E-16	0.1705	
1.5-85-1	0.785	0.167	4.59E-16		Dried (see Table 3)
1.5-85-2	0.794	0.157	6.32E-16	0.1826	
1.5-90-1	0.870	0.098	1.94E-16		Dried (see Table 3)
1.5-90-2	0.863	0.103	1.03E-16	0.1702	
1.6-10-1	0.101	0.626	5.78E-16	0.1572	
1.6-15-1	0.179	0.524	5.39E-16		Wetted (see Table 3)
1.6-20-1	0.271	0.469	5.02E-16	0.1306	
1.6-30-1	0.339	0.422	5.07E-16		Wetted (see Table 3)
1.6-40-2	0.409	0.383	4.72E-16	0.1336	
1.6-50-1	0.490	0.328	4.11E-16	0.1441	
1.6-60-1	0.581	0.272	3.39E-16	0.1195	
1.6-70-2	0.663	0.213	2.51E-16	0.1137	
1.6-80-1	0.752	0.158	1.46E-16	0.1266	
1.7-10-1	0.100	0.497	2.53E-16	0.1347	
1.7-20-1	0.211	0.425	3.22E-16		Wetted+dried (see Table 3)
1.7-30-1	0.319	0.366	2.73E-16	0.1317	
1.7-40-1	0.401	0.320	2.34E-16	0.0995	
1.7-50-2	0.475	0.292	2.96E-16		Wetted (see Table 3)
1.7-60-1	0.580	0.227	1.84E-16	0.0890	
1.7-70-1	0.698	0.164	9.42E-17		Dried (see Table 3)
1.7-80-2	0.783	0.116	7.78E-17	0.0951	

Table 3. Effective air permeability and pore size parameters for specimens subjected to wetting and drying paths

Specimen ID	Path	S_r	e_a	k_{eff}	PSP
		(-)	(-)	(m^2)	(-)
1.1-10-1	Initial	0.117	1.239	1.52E-14	
	Wet01	0.254	1.058	1.39E-14	
	Wet02	0.323	0.952	1.37E-14	
	Wet03	0.577	0.531	7.85E-15	
	Wet04	0.631	0.441	6.70E-15	0.2596
1.1-20-2	Initial	0.192	1.114	2.07E-14	
	Wet01	0.269	1.022	2.00E-14	
	Wet04	0.607	0.501	9.26E-15	
	Wet05	0.728	0.313	3.90E-15	0.2390
1.1-30-2	Initial	0.300	0.965	3.65E-14	
	Wet01	0.379	0.873	3.54E-14	
	Wet03	0.642	0.458	1.30E-14	
1.1-40-2	Initial	0.401	0.818	1.25E-13	
	Wet02	0.576	0.573	6.30E-14	
	Wet03	0.716	0.345	1.76E-14	0.4440
1.1-50-3	Initial	0.485	0.701	6.71E-13	
	Dry01	0.069	1.203	7.29E-13	
	Dry02	0.038	1.242	7.00E-13	0.9748
1.3-10-2	Initial	0.089	0.960	3.29E-15	
	Wet01	0.341	0.720	3.78E-15	
	Wet02	0.392	0.660	3.62E-15	
	Wet03	0.492	0.540	3.22E-15	
	Wet05	0.692	0.310	1.46E-15	
	Wet06	0.830	0.170	1.20E-16	
	Wet07	0.869	0.128	4.49E-17	0.1926
1.3-80-2	Initial	0.793	0.203	3.82E-13	
	Dry01	0.218	0.624	5.66E-13	
	Dry02	0.060	0.753	7.34E-13	0.6465
1.5-10-2	Initial	0.108	0.716	1.09E-15	
	Wet01	0.367	0.528	1.19E-15	
	Wet02	0.684	0.266	4.81E-16	
	Wet03	0.840	0.135	1.36E-16	
	Wet04	0.907	0.078	2.08E-17	0.1538
1.5-30-2	Initial	0.314	0.539	1.11E-15	
	Wet01	0.430	0.461	1.23E-15	
	Wet02	0.518	0.395	1.06E-15	
	Wet03	0.595	0.333	8.57E-16	
	Wet04	0.689	0.262	5.16E-16	
	Wet05	0.814	0.157	1.24E-16	
	Dry01	0.899	0.079	1.74E-17	
	Dry02	0.815	0.143	5.64E-17	
	Dry03	0.754	0.186	7.62E-17	
	Dry04	0.707	0.223	1.93E-16	

	Dry05	0.656	0.259	2.99E-16	
	Dry06	0.542	0.340	5.60E-16	
	Dry07	0.439	0.413	6.53E-16	
	Dry08	0.363	0.465	7.79E-16	
	Dry09	0.254	0.553	2.08E-15	0.1748
1.5-50-2	Initial	0.424	0.455	1.59E-15	
	Wet01	0.575	0.350	1.27E-15	
	Wet02	0.632	0.307	1.13E-15	
	Wet03	0.697	0.257	7.53E-16	
	Wet04	0.833	0.144	1.93E-16	
	Wet05	0.979	0.018	0.00E+00	
	Dry01	0.952	0.042	2.38E-17	
	Dry02	0.889	0.092	5.73E-17	
	Dry04	0.821	0.142	5.45E-17	
	Dry05	0.756	0.191	9.93E-17	
	Dry06	0.634	0.282	3.88E-16	
	Dry07	0.425	0.434	8.42E-16	0.1485
1.5-60-2	Initial	0.535	0.363	1.48E-15	
	Wet01	0.642	0.292	1.13E-15	
	Wet02	0.704	0.245	8.68E-16	
	Wet03	0.768	0.194	5.54E-16	
	Wet04	0.839	0.138	2.18E-16	
	Wet05	0.871	0.111	1.74E-16	
1.5-70-2	Initial	0.628	0.290	1.25E-15	
	Wet01	0.686	0.253	1.04E-15	
	Wet02	0.761	0.198	7.01E-16	
	Wet03	0.826	0.147	2.95E-16	
	Wet04	0.873	0.109	1.08E-16	
	Wet05	0.903	0.083	4.04E-17	
	Wet06	0.944	0.049	1.51E-17	
	Wet07	0.964	0.032	1.15E-17	0.0846
1.5-85-1	Initial	0.785	0.167	4.59E-16	
	Dry01	0.341	0.478	1.63E-15	
	Dry02	0.076	0.670	2.66E-15	
	Dry03	0.075	0.673	2.81E-15	0.2349
1.5-90-1	Initial	0.870	0.098	1.94E-16	
	Dry01	0.828	0.126	1.80E-16	
	Dry02	0.739	0.184	3.09E-16	
	Dry03	0.682	0.221	4.02E-16	
	Dry04	0.615	0.266	6.61E-16	
	Dry05	0.550	0.310	7.45E-16	
	Dry06	0.489	0.354	8.47E-16	
	Dry07	0.315	0.472	1.30E-15	
	Dry08	0.202	0.553	2.76E-15	0.1872
1.6-15-1	Initial	0.179	0.524	5.39E-16	
	Wet01	0.281	0.474	6.81E-16	
	Wet02	0.344	0.435	6.19E-16	

	Wet03	0.418	0.391	7.25E-16	
	Wet04	0.513	0.330	4.70E-16	
	Wet05	0.580	0.285	5.12E-16	
	Wet06	0.671	0.227	2.92E-16	
	Wet07	0.780	0.153	1.13E-16	
	Wet08	0.854	0.103	4.27E-17	
	Wet09	0.911	0.063	1.82E-17	0.0619
1.6-30-1	Initial	0.339	0.422	5.07E-16	
	Wet01	0.377	0.403	6.40E-16	
	Wet02	0.515	0.323	6.21E-16	
	Wet03	0.581	0.280	4.36E-16	
	Wet04	0.607	0.263	3.93E-16	
	Wet05	0.752	0.170	1.68E-16	
	Wet06	0.917	0.059	4.15E-18	
1.7-20-1	Initial	0.211	0.425	3.22E-16	
	Wet01	0.237	0.417	3.86E-16	
	Wet02	0.306	0.385	4.41E-16	
	Wet03	0.388	0.344	3.52E-16	
	Wet04	0.489	0.291	3.64E-16	
	Wet05	0.582	0.242	2.35E-16	
	Wet06	0.662	0.198	1.48E-16	
	Wet07	0.771	0.134	7.06E-17	
	Wet08	0.838	0.097	3.25E-17	
	Dry01	0.597	0.230	1.33E-16	
	Dry02	0.343	0.369	1.35E-15	
	Dry03	0.193	0.454	3.15E-15	0.1314
1.7-50-2	Initial	0.475	0.292	2.96E-16	
	Wet01	0.501	0.282	2.62E-16	
	Wet02	0.627	0.216	1.86E-16	
	Wet03	0.768	0.138	6.96E-17	0.0733
1.7-70-1	Initial	0.698	0.164	9.42E-17	
	Wet01	0.688	0.172	1.28E-16	
	Wet02	0.725	0.154	2.49E-16	
	Wet03	0.802	0.115	5.78E-17	
	Wet04	0.888	0.068	2.19E-17	
	Dry01	0.534	0.257	1.70E-16	
	Dry02	0.347	0.358	3.55E-16	

Appendix

A new approach for estimating the pore size parameter PSP, the key ingredient in the capillary model proposed by Garcia-Bengochea et al. (1979), is described here. As in the original model by García-Bengoechea et al., the derivation presented below is based on the following assumptions:

- The porous media is modelled as a set of parallel cylindrical tubes of constant radius along its length;

- The radius of each tube varies as a function of the pore size distribution (PSD) (estimated here from MIP tests);
- The number of tubes with the same radius ri is estimated from the volumetric frequency curve, calculated using the incremental volume data from the intrusion stage in MIP tests.
- The flow rate of fluid through the porous media is equivalent to the summation of the flow rates through each capillary tube in the medium.

García-Beogoechea et al. (1979) adopted the Hagen-Poiseuille equation to represent the flow of water through the porous media. However, this expression seems not to properly represent the flow of gas through the compacted clay. Therefore, the Darcy-Weisbach equation is adopted here as it may be employed to simulate the head loss in circular pipes even for cases of compressible fluids where the variation in gas density is small (e.g., air conducts) (e.g., Sweemee and Jani, 1976; Brown, 2002). In terms of a pressure drop form, the Darcy-Weisbach equation is given by:

$$\Delta p = f \cdot \frac{L\rho}{2} \cdot \frac{v^2}{D} \quad \text{(A1)}$$

where Δp is the pressure drop [Pa], f is the friction factor, D is the diameter of the pipe [m], L is the length of the pipe [m], v is the mean flow velocity [m/s] and ρ is the density of the fluid [kg/m^3].

Eq. A1 can be rewritten in terms of the volumetric flow rate by substituting Q= $A \cdot v$, with $A = \pi \frac{D^2}{4}$, which leads to:

$$\frac{\Delta p}{L} = f \cdot \frac{8\rho}{\pi^2} \cdot \frac{Q^2}{D^5} \quad \text{(A2)}$$

Eq. A2 can be re-written in terms of the radius of the pipe as:

$$\frac{\Delta p}{L} = f \cdot \frac{\rho}{\pi^2} \cdot \frac{q^2}{4r^5} \quad \text{(A3)}$$

Therefore, the volumetric flow rate for one capillary tube of radius r_i is given by:

$$Q_i = 2 \cdot \sqrt{\frac{\Delta p}{L}} \cdot \sqrt{\frac{1}{\rho f}} \cdot \pi r_i^2 \cdot \sqrt{r_i} \quad \text{(A4)}$$

The flow rate through all n_i capillary tubes of radius r_i is estimated as $Q_i=n_i.q_i$. Hence, the flow rate through the whole medium is expressed by:

$$Q = \sum_{i=1}^{N} Q_i \quad \text{(A5)}$$

which leads to

$$Q = 2 \cdot \sqrt{\frac{\Delta p}{L}} \cdot \sqrt{\frac{1}{\rho f}} \cdot \sum_{i=1}^{N} n_i \cdot \pi r_i^2 \cdot \sqrt{r_i} \quad \text{(A6)}$$

By replacing $Q = v_s A$, with v_s =seepage velocity and A = total cross-section area, Eq. A6 leads to:

$$v_S = \frac{Q}{A} = 2 \cdot \sqrt{\frac{\Delta p}{L}} \cdot \sqrt{\frac{1}{\rho f}} \cdot \sum_{i=1}^{N} \frac{n_i \cdot \pi r_i^2}{A} \cdot \sqrt{r_i} \quad \text{(A7)}$$

The proportion of the cross-section area, A, that corresponds to capillary tubes of radius r_i is named as $\alpha(r_i) = \frac{n_i \cdot \pi r_i^2}{A}$. This value is equal to the volumetric frequency $\sum_{i=r_{min}}^{r_{max}} f(r_i)$ for capillary tubes with radius r_i. Hence, Eq. A7 may be re-written as:

$$v_S = 2 \cdot \sqrt{\frac{\Delta p}{L}} \cdot \sqrt{\frac{1}{\rho f}} \cdot \sum_{i=r_{min}}^{r_{max}} f(r_i) \cdot \sqrt{r_i} \quad \text{(A8)}$$

The mean flow velocity in a unit medium is calculated as $v = n \cdot v_s$ (where n is porosity) which leads to:

$$v = 2 \cdot \sqrt{\frac{\Delta p}{L}} \cdot \sqrt{\frac{1}{\rho f}} \cdot n \cdot \sum_{i=r_{min}}^{r_{max}} f(r_i) \cdot \sqrt{r_i} \quad \text{(A9)}$$

By introducing the Darcy's law $v = \frac{k}{\mu_a} \cdot \frac{\Delta P}{L}$ into Eq. 7 (μ_a being the dynamic viscosity of the fluid), we obtain:

$$\frac{k}{\mu_a} \cdot \frac{\Delta P}{L} = 2 \cdot \sqrt{\frac{\Delta p}{L}} \cdot \sqrt{\frac{1}{\rho f}} \cdot n \cdot \sum_{i=r_{min}}^{r_{max}} f(r_i) \cdot \sqrt{r_i} \quad \text{(A10)}$$

or

$$k = 2 \cdot \sqrt{\frac{L}{\Delta P}} \cdot \frac{\mu_a}{\sqrt{\rho f}} \cdot n \cdot \sum_{i=r_{min}}^{r_{max}} f(r_i) \cdot \sqrt{r_i} \quad \text{(A11)}$$

This expression can be rearranged following García-Bengoechea et al. (1979), in the form:

$$k = C_S \cdot PSP \quad \text{(A12)}$$

where: C_S is a shape factor, $C_S = 2 \cdot \sqrt{\frac{L}{\Delta P}} \cdot \frac{\mu_a}{\sqrt{\rho f}}$ and PSP is the pore size parameter, estimated defined as

$$PSP = n \cdot \sum_{i=r_{min}}^{r_{max}} f(r_i) \cdot \sqrt{r_i} \quad \text{(A13)}$$

In Eq. A13, the volumetric frequency $f(r_i)$ is multiplied by the squared root of the radius r_i. It corresponds to an exponent alpha equal to 0.5 which provides the best fitting of the experimental data as shown in Figure 24.

References

Alonso E.E., Pinyol N. & Gens A. (2013) Compacted soil behaviour: initial state, structure and constitutive modelling. Geotechnique, 63(6), 463-478.

Barden L. and Sides G.R. (1970) Engineering behaviour and structure of compacted clay. Journal of the Soil Mechanics and Foundation Division, ASCE 96(4), 1171-1200.

Barden L., McGown A. and Collins K. (1973) The collapse mechanism in partly saturated soil. Engineering Geology, 7(1), 49-60.

Blatz, J. A., Cui, Y.-J. & Oldecop, L. (2008). Vapour equilibrium and osmotic technique for suction control. Geotech. Geol. Engng 26, No. 6, 661 – 673.

Brown, G. O. (2002). The History of the Darcy-Weisbach Equation for Pipe Flow Resistance. ASCE Civil Engineering Conference and Exposition 2002. Washington, D.C., United States, American Society of Civil Engineers, 34-43.

Casagrande A. (1932) The structure of clay and its importance in foundation engineering. Journal Boston Society of Civil Engineers, 19, 168-209.

Chandler, R.J., Crilly, M.S. & Montgomery-Smith (1992) A low-cost method of assessing clay desiccation for low-rise buildings. Proc. Instn. Civ. Engng, 92;2; 82-89.

Chamindu Deepagoda, T.K.K., Moldrup, P., Schjønning, P., Lis Wollesen de Jonge, Kawamotoc, K., and Komatsu, T. (2011) Density-corrected models for gas diffusivity and air permeability in unsaturated soil. Vadose Zone Journal, 10(1): 226–238.

Chen C., Zhang D. and Zhang J. (2017) Influence of stress and water content on air permeability of intact loess. Canadian Geotechnical Journal, 54: 1221-12230.

Coussy, O. (1995). Mechanics of porous continua. Chichester, UK:Wiley.

Diamond, S. (1970). Pore size distributions in clays. Clays and Clay Minerals 18, No. 1, 7–23.

Delage, P., & Lefebvre, G. (1984). Study of the structure of a sensitive Champlain clay and of its evolution during consolidation. Canadian Geotechnical Journal, 21(1), 21–35. doi:10.1139/t84-003

Delage, P. & Pellerin, M. 1984. Influence de la lyophilisation sur la structure d'une argile sensible du Quebec, Clay Minerals, 19: 151-160. doi:10.1180/claymin.1984.019.2.03

Delage, P., Audiger, M., Cui, Y. J. & Howat, M. (1996). Microstructure of a compacted silt. Can. Geotech. J. 33, No. 1, 150–158.

Delage, P., Marcial, D., Cui, Y., & Ruiz, X. (2006). Ageing effects in a compacted bentonite: a microstructure approach. Géotechnique, 56(5), 291–304.

Garcia-Bengoechea I., Altschaefll A.G. and Lovell C.W. (1979) Pore distribution and permeability of silty clays. Journal of Geotechnical Engineering Division 105(7), 839-856.

He Y., Cui Y-J., Ye W-M. and Conil N. (2017) Effects of wetting-drying cycles on the air permeability of of compacted Téguline clay. Engineering Geology, 228, 173-179.

Juang C.H. and Holtz R.D. (1986) Fabric, Pore Size Distribution and Permeability of Sandy Soils. Journal of Geotechnical Engineering 112(9), 855-868.

Juca J.and Maciel F. (2006) Gas permeability of a compacted soil used in a landfill cover layer. In Proc. UNSAT2006, Carefree, Arizona, United States, ASCE, 1435-1446.

Lambe T.W. (1953) The structure of inorganic soils. Proc. American Society of Civil Engineers, Separate No. 315, 1-49.

Lambe T.W. (1958a) The structure of compacted clay. Journal of the Soil Mechanics and Foundation Division, ASCE, 84(SM2), 1654-1 through 1654-34.

Lambe T.W. (1958b) The engineering behaviour of compacted clay. Journal of the Soil Mechanics and Foundation Division, ASCE, 84(SM2), 1655-1 through 1655-35.

Leonards G. A. (1955) Strength characteristics of compacted clays. Trans. ASCE 120, 1420-1454

Liu J.F., Skoczylas F. and Talandier J. (2015) Gas permeability of a compacted bentonite-sand mixture: coupled effects of water content, dry density and confining pressure. Canadian Geotechnical Journal, 52: 1159-1167.Mitchell J.K., Hooper D. and Campanella R. (1965) Permeability of compacted clay. Journal of the Soil Mechanics and Foundations Division 91(4), 41-66.
McGown A. and Collins K. (1975) The microfabrics of some expansive and collapsing soils. Proc. 5th Panamerican Conf. Soil Mech. And Foundation Engineering, Buenos Aires, Argentina, Vol 1, pp. 323-332.
Moldrup, P., Yoshikawa, S., Olesen, T., Komatsu, T., and Rolston, D.E. 2003. Air permeability in undisturbed volcanic ash soils: predictive model test and soil structure fingerprints. Soil Science Society of America Journal, 67(1): 32–40.
Monroy, R., Zdravkovic, L. & Ridley, A. (2010). Evolution of microstructure in compacted London clay during wetting and loading. Geotechnique 60, No. 2, 1051-119.
Osipov V.I. and Sokolov V.N. (1978) A study on the nature of the strength and deformation properties of clay soils with the help of the scanning electron microscope. Bull Eng. Geol. Environ., 17(1), 91-94.
Olivella S. and Alonso E.E. (2008) Gas flow through clay barriers. Geotechnique, 58(3), 157-176.
Pineda J.A., Romero E., Alonso E.E. and Pérez T. (2014) A new high-pressure triaxial apparatus for inducing and tracking hydro-mechanical degradation of clayey rocks. Geotechnical Testing Journal, 37(6), 933-947.
Romero E., Gens A. and Lloret A. (1999) Water permeability, water retention and microstructure of unsaturated compacted Boom clay. Engineering Geology, 54, 117-127.
Romero E., Garcia I. and Knobelsdorf J. (2005) Gas permeability evolution of a sand/bentonite during controlled-suction paths. Advanced Experimental Unsaturated Soil Mechanics, EXPERUS2005, Trento, Italy, Tarantino, Romero & Cui (eds), Balkema, 385-390.
Romero E. and Simms P. (2008) Microstructure investigation in unsaturated soils: a review with special attention to contribution of mercury intrusion porosimetry and environmental scanning electron microscopy. Geotechnical and Geological Engineering, 26(6), 705-727.
Romero E. (2013) A microstructural insight into compacted clayey soils and their hydraulic properties. Engineering Geology, 165(1), 3-19.
Seed H.B. and Chan C.K. (1959) Structure and strength characteristics of compacted clay. Journal of the Soil Mechanics and Foundation Division, ASCE, 84(SM5), 87-128.
Sridharan A., Altschaeffl A. G. & Diamond S. (1971). Pore size distribution studies. J. Soil Mech. Found. Div. 97, No. SM5, 771-787
Swamee, P. and A. K. Jain (1976). "Explicit equations for pipe-flow problems." Journal of the hydraulics division 102: 657-664.
Tarantino, A. & de Col, E. (2008). Compaction behaviour of clay. Geotechnique 58, No. 3, 199-214.
Terzaghi K. (1925) Modern conceptions concerning foundation engineering. Journal Boston Society of Civil Engineers, 12(10), 1-43.
Vanpaisal T. Bouazza A. (2004) Gas permeability of partially hydrated geosynthetic clay liners. Journal of Geotechnical and Geoenvironmental Engineering, 130(1), 93-102.
Villar M.V., Romero E.. and Lloret A. (2005) Thermo-mechanical and geochemical effects on the permeability of high-density clays. In Proc. Advances in understanding engineered clay barriers: proceedings of the International Symposium on Large Scale Field Tests in Granite, Sitges, Barcelona, Spain, Balkema, Rotherdam, 177-191.
Washburn, E. W. (1921). Note on a method of determining the distribution of pore sizes in a porous material. Proc. Natn. Acad. Sci. USA 7, No. 4, 115–116.
Yoshimi J. and Osterberg J.O. (1963) Compression of partially saturated cohesive soils. Journal of the Soil Mechanics and Foundations Division ASCE, 89(4), 1-24.
Zhan T., Yang Y., Chen R., Ng C. and Chen Y.M. (2014) Influence of clod size and water content on gas permeability of a compacted loess. Canadian Geotechnical Journal, 51(12), 1468-1474.